Accepted Manuscript

Late Neoarchean crust-mantle geodynamics: Evidence from Pingquan Complex of the Northern Hebei Province, North China Craton

Wei Wang, Shuwen Liu, Peter A. Cawood, Rongrong Guo, Xiang Bai, Boran Guo

PII: S0301-9268(16)30341-2
DOI: http://dx.doi.org/10.1016/j.precamres.2017.06.007
Reference: PRECAM 4789

To appear in: *Precambrian Research*

Received Date: 23 August 2016
Revised Date: 6 May 2017
Accepted Date: 12 June 2017

Please cite this article as: W. Wang, S. Liu, P.A. Cawood, R. Guo, X. Bai, B. Guo, Late Neoarchean crust-mantle geodynamics: Evidence from Pingquan Complex of the Northern Hebei Province, North China Craton, *Precambrian Research* (2017), doi: http://dx.doi.org/10.1016/j.precamres.2017.06.007

Late Neoarchean crust-mantle geodynamics: Evidence from Pingquan Complex of the Northern Hebei Province, North China Craton

Wei Wang[a,b,c,*], Shuwen Liu[b,*], Peter A. Cawood[c,d], Rongrong Guo[e], Xiang Bai[f], Boran Guo[b]

[a] The State Key Laboratory of Geological Processes and Mineral Resources, School of Earth Sciences and Resources, China University of Geosciences, Beijing 100083, PR China

[b] The Key Laboratory of Orogenic Belts and Crustal Evolution, Ministry of Education, School of Earth and Space Sciences, Peking University, Beijing 100871, PR China

[c] Department of Earth Sciences, University of St. Andrews, North Street, St. Andrews KY16 9AL, UK

[d] School of Earth, Atmosphere and Environment, Monash University, Victoria 3800, Australia

[e] Department of Geology, College of Resources and Civil Engineering, Northeastern University, Shenyang 110819, China

[f] Key Laboratory of Active Tectonics and Volcano, Institute of Geology, China Earthquake Administration, Beijing 100029, China

Corresponding authors:

* Wei Wang, School of Earth Sciences and Resources, China University of Geosciences, Beijing 100083, China; Email: sanyechong198819@163.com / wangw1988@cugb.edu.cn

* Shuwen Liu, School of Earth and Space Sciences, Peking University, Beijing 100871, China; Tel/Fax: 86-10-62754163; Email: swliu@pku.edu.cn

Abstract A late Neoarchean intra-oceanic arc along the northwestern margin of Eastern Block (EB), North China Craton, provides important insights into the nature of Archean mantle sources and crust-mantle geodynamics. The Pingquan Complex and the entire Northern Hebei Province (NHB) are located in the middle part of the arc, and overlap the northern extent of the Trans-North China Orogen. Zircon U-Pb isotopic age data reveal that the Pingquan Complex consists of ~2537-2515 Ma dioritic gneisses, ~2506-2503 Ma amphibolites, and ~2491 Ma quartz monzodioritic to monzogranitic gneisses, and they show dominantly positive zircon εHf(t) (-0.6-+5.4) that are lower than coeval model depleted mantle values.

Geochemical data for the Pingquan rocks and synchronous metabasalts and granitoid gneisses of Huai'an-Xuanhua and Dantazi complexes in the NHB are integrated. Except for the monzogranitic gneisses that were derived from partial melting of juvenile metagreywackes, the other rocks of the Pingquan Complex were derived from a metasomatized lithospheric mantle, and subjected to variable fractionation of clinopyroxene, hornblende and plagioclase, without significant crustal contamination. Moderately depleted zircon εHf(t), and high Sm/Hf and Nb/Ta (mostly of 1.34-3.96 and 15.50-32.58) suggest that the lithospheric mantle was enriched by subducted pelagic sediments metamorphosed to rutile-bearing eclogites before melting.

Late Neoarchean crust-mantle geodynamic processes in the NHB are reconstructed. Intra-oceanic subduction initiated offshore of the northwestern margin of the EB at ~2.55 Ga or earlier. Partial melting of slab basalts occurred at ~2542-2499 Ma, with the melts contaminated by mantle wedge materials forming TTGs. Meanwhile, the sub-arc lithospheric mantle was enriched by fluids and melts released from slab basalts and pelagic sediments, and partial melting of this moderately depleted mantle generated ~2537-2503 Ma diorites and basalts. Following final accretion of the arc onto the continental margin of the EB, the slab rollback/breakoff and asthenospheric mantle upwelling triggered partial melting of the metasomatized lithospheric mantle and crustal anatexis, generating ~2491 Ma quartz monzodioritic and monzogranitic rocks.

Accordingly, the NHB records Neoarchean crustal growth linked to oceanic subduction and arc-continent accretion, and highlights the importance of resolving the nature of mantle sources and crust-mantle interactions in understanding Archean crustal growth and evolution.

Keywords: Late Neoarchean crustal growth; sediment recycling and crust-mantle interaction; arc-continent accretion; Pingquan Complex of Northern Hebei Province; North China Craton

1. Introduction

For the Archean period, there are still many uncertainties in crustal growth and evolution due to enigmatic nature and evolution of the depleted mantle, which directly influence the crustal growth and reworking history established from Lu-Hf or Sm-Nd depleted mantle model ages (Rollinson, 2010; Dhuime et al., 2011; Griffin et al., 2014; Payne et al., 2016; Vervoort and Kemp, 2016). Short-lived ^{146}Sm-^{142}Nd and zircon Lu-Hf isotopes revealed chondritic or depleted Hadean mantle, leading to contrasting models of early crust-mantle differentiation (O'Neil et al., 2008, 2016; Caro and Bourdon, 2010; Kemp et al., 2010; Zeh et al., 2014; Hiess and Bennett, 2016). Eoarchean (ultra-)depleted mantle domains have been identified, but may have been more extensive because they were gradually eliminated by mantle overturns or crustal recycling (Hoffmann et al., 2010; Dhuime et al., 2012, 2015; Khanna et al., 2014; Wang et al., 2015a). Crustal recycling at destructive plate margins could have been a common feature since the onset of plate tectonics possibly at ~3.2-3.0 Ga (Dhuime et al., 2012, 2015). Due to the contribution of subducted sediments, new crust produced at island arcs show $\varepsilon Hf(t)$ values lower than the coeval depleted mantle values, and the calculated depleted mantle model ages from the island arc rocks are apparently older than the actual timing of crustal growth (Dhuime et al., 2011). In the case of a post-collisional setting, despite enriched zircon $\varepsilon Hf(t)$ values and older depleted mantle model ages of the mafic rocks and their derivatives, crust-mantle interaction studies reveal that they record significant crustal growth (Couzinié et al., 2016). Accordingly, the nature and evolution of regional mantle sources and crust-mantle interactions are critical for unraveling Archean crustal growth and evolution as well as geodynamics.

The North China Craton (NCC) displays a complex early Precambrian evolutionary history (Fig. 1A; Zhao et al., 1998, 2005, 2012; Guo et al., 2002, 2012; Liu et al., 2008; Wan et al., 2010, 2013, 2014; Zhai and Santosh, 2011, 2013). Controversies yet to be resolved are whether the major ~2.6-2.5 Ga tectonothermal events record crustal growth or reworking, and the nature of the associated geodynamic regime (Zhao et al., 1998, 2005; Geng et al., 2010; Liu et al., 2011a, 2013; Nutman et al., 2011; Wang and Liu, 2012; Wang et al., 2015b, 2016).

In this contribution, we provide zircon U-Pb and Lu-Hf isotopes, and whole-rock geochemical data for a suite of Neoarchean amphibolites, dioritic gneisses, and potassium-rich granitoid gneisses from the Pingquan Complex, Northern Hebei Province, along the northern margin of the NCC (Fig. 1B). Combined with crust-mantle interactions deduced from the ~2.6-2.5 Ga intra-oceanic arc system along northwestern margin of Eastern Block (Fig. 1B; Wang et al., 2015b), we propose that sediment recycling has contributed to mantle heterogeneity beneath this ancient arc system, and this has significant implications for reconstructing the Archean crustal growth and evolution of the North China Craton.

2. Geological background

The North China Craton is divided into Eastern Block (EB) and Western Block (WB) which were juxtaposed along the Trans-North China Orogen (TNCO) at ~1.85 Ga (Fig. 1A; Zhao et al., 1998, 2005, 2012; Guo et al., 2002, 2005; Liu et al., 2002, 2006, 2012a). The Western Block was divided into the Yinshan Block and the Ordos Block that were consolidated via the Khondalite Belt (or "Inner Mongolia Suture Zone") at ~1.92 Ga, and the Eastern Block witnessed Paleoproterozoic rifting and subduction-collision events, forming the Jiao-Liao-Ji

Belt (Li and Zhao, 2007; Santosh et al., 2007; Guo et al., 2012; Liu et al., 2014).

The Eastern Block is the major archive of Archean basement terranes in the NCC (Fig. 1B). Based on ~2.7 Ga komatiites in Western Shandong, anti-clockwise metamorphic P-T-t paths of mafic granulites, and pervasive ~2.55-2.50 Ga granitoid gneisses, some researchers have proposed formation of the block in a mantle plume setting (Zhao et al., 1998, 2005; Geng et al., 2010; Wu et al., 2016a). Compilations of whole-rock Sm-Nd or zircon Lu-Hf isotopic model ages reveal ~2.7 Ga crustal growth along with crustal reworking at ~2.5 Ga (Wu et al., 2005; Geng et al., 2012; Wang and Liu, 2012). Alternatively, a Neoarchean subduction-related arc setting was advocated for the northern margin of the EB as well as for some of the Neoarchean complexes that have been involved in the Paleoproterozoic TNCO (Liu et al., 2002, 2004, 2011a; Diwu et al., 2011; Kusky, 2011; Nutman et al., 2011; Wang et al., 2011, 2012a, 2013, 2015b, 2016; Guo et al., 2013, 2015a,b; Bai et al., 2014a, 2016; Deng et al., 2016). In particular, a ~2.6-2.5 Ga intra-oceanic arc was proposed to have formed along northwestern EB, marking a pulse of intense crustal growth within the craton (Wang et al., 2015b).

As proposed by Wang et al. (2015b), the Northern Hebei province (NHB) is located in the middle segment of the newly established Neoarchean intra-oceanic arc, which also overlaps the northern extent of the late Paleoproterozoic TNCO (Fig. 1; Zhao et al., 2005). From southwest to northeast, the Neoarchean basement of NHB comprises the Huai'an-Xuanhua, the Dantazi, and the Pingquan complexes. The Huai'an-Xuanhua Complex consists of dioritic and tonalite-trondhjemite-granodiorite (TTG) gneisses, with smaller volumes of supracrustal rocks (Guo et al., 2002, 2005; Zhao et al., 2008, 2010; Liu et al., 2012b). Magmatic precursors of the granitoid gneisses were emplaced at ~2.55-2.50 Ga, and they were subsequently intruded by potassic granites at ~2.49 Ga, ~2.44 Ga, and ~2.0 Ga (Zhang et al., 2011; Liu et al., 2012b). All these lithologies were overprinted by ~1.85 Ga granulite facies metamorphism, forming high-pressure mafic granulites and charnockitic to S-type granites (Guo et al., 2002, 2005, 2015c; Zhao et al., 2008, 2010; Wu et al., 2016b). The Neoarchean Chengde Complex has been commonly known as the “Dantazi Complex”, and is separated from the Paleoproterozoic Hongqiyingzi Complex in the north by the Chongli-Damiao Fault (Fig. 1B; Liu et al., 2007a,b, 2011b). The Dantazi Complex is composed chiefly of ~2517-2473 Ma TTG and monzogranitic gneisses with minor ~2600-2530 Ma supracrustal rocks, which were subjected to granulite facies metamorphism at ~2427-2404 Ma and ~1834-1793 Ma, respectively (Liu et al., 2007a, 2011b; Zhang et al., 2016). Some low grade ~2502-2490 Ma basalts, andesites, and dacites have also been identified in the Dantazi Complex (Ge et al., 2015).

The Pingquan Complex is located at the eastern part of the NHB, connecting the TNCO and EB (Zhao et al., 2005). Early 1:200,000 scale geological mapping (Hebei Regional Geological Survey Team) divided the early Precambrian basement rocks into the lower Qianxi Group and the upper Dantazi Group, which were considered to be separated by an angular unconformity. The Qianxi Group consists of amphibolites, hornblende plagioclase leptytites, and biotite hornblende plagioclase gneisses, intercalated with minor marbles in the base and some garnet two pyroxene plagioclase granulites and banded iron formations (BIFs) towards the inferred top of succession. The Dantazi Group is composed of biotite leptytites and hornblende plagioclase gneisses. However, later studies indicated that the “unconformity” is a tectonic feature, invalidating the previous proposed stratigraphy (Tan et al., 1991).

Granulite-facies metamorphic rocks occur locally in the Wudaohe area and record a peak metamorphic P-T condition of 707-790 °C and 8.56 kbar. They are marked by a gneissic dome structure. Metamorphosed domains of amphibolite facies in the Pingquan Complex are characterized by a series of fold belts with NW-dipping axial planes, which are punctuated by Mesozoic granitoid plutons or volcano-sedimentary sequences. Peak metamorphic P-T condition of 670 °C and 7 kbar was documented by Tan et al. (1991). Based on our field investigation, granitoid gneisses are the main lithologies in the Pingquan Complex, and supracrustal metavolcanic rocks are mainly distributed in the Chagou and Qigou areas (Fig. 2). In the Chagou area, voluminous amphibolites alternate with BIFs (Fig. 3A). Dioritic gneisses show intense gneissosity, and are widely intruded by gneissic monzogranitic bodies (Fig. 3B-C). Due to regional deformation, these monzogranitic bodies are parallel with the gneissosity of dioritic gneisses (Fig. 3C). Geological relationships between supracrustal amphibolites and (quartz) dioritic gneisses were obliterated by intense mylonitization. Quartz monzodioritic and monzogranitic gneisses are widely developed in the Pingquan area, and locally intrude the dioritic gneisses (Fig. 3D-F). They represent the latest Archean tectonothermal events, and contain enclaves of dioritic gneisses and amphibolites (Fig. 3E).

Basement rocks of NHB are variably affected by late Paleoproterozoic to Mesoproterozoic extension-related magmatism, Paleozoic orogenesis, which is focused in the Central Asian Orogenic Belt to the north, and Mesozoic magmatism caused by lithospheric thinning in the Eastern China. These tectonothermal events led to the formation of Proterozoic mafic dykes, gabbro-anorthosite suites, and alkaline granitoids, Meso- to Neoproterozoic sedimentary cover sequences, as well as Phanerozoic (volcano-)sedimentary sequences and granitoid plutons (Peng et al., 2008; Zhao et al., 2012; Xu et al., 2013; Wang et al., 2015c).

3. Sampling and petrology

Twenty-two representative samples were collected from Pingquan Complex: nine amphibolites, four dioritic gneisses, five quartz monzodioritic gneisses, and four monzogranitic gneisses (Supplementary Table 1). Amphibolites consist chiefly of hornblende (45-55%) and plagioclase (45-50%), with accessory epidote, magnetite, zircon, and apatite (Fig. 4A-B). They display medium- to fine-grained textures and gneissic structures, and the mylonitized amphibolites show banded structures defined by separate hornblende and plagioclase domains (Fig. 4C). Most dioritic gneisses display fine-grained porphyroblastic textures and intense gneissic structures, with fine granulation and dynamic recrystallization (Fig. 4D-E). The major minerals are clinopyroxene (18-25%), orthopyroxene (12-15%), plagioclase (52-55%), hornblende (5-8%), and minor quartz, with accessory zircon, magnetite, and apatite. The close paragenesis of orthopyroxene and clinopyroxene suggests local granulite-facies metamorphic grade (Fig. 4E). Some samples were subjected to retrograde metamorphism, and hornblende and chlorite serve as the major mafic minerals. The quartz dioritic gneiss sample 13PQ18-1 shows coarse-grained texture and gneissic structure, and consists of plagioclase (~65%), quartz (~12%), hornblende (~12%), biotite (~5%), minor orthopyroxene, and accessory epidote, zoisite, apatite, zircon, and magnetite (Fig. 4F). The medium- to fine-grained quartz monzodioritic gneisses are composed mainly of plagioclase (50-55%), biotite (12-15%), K-feldspar (8-12%), hornblende (5-10%), and quartz (10-15%) (Fig. 4G). The monzogranitic gneisses have medium- to coarse-grained textures and gneissic structures (Fig. 4H).

Plagioclase (35-45%), K-feldspar (25-30%, perthite and microcline), and quartz (25-30%) are the major minerals, with minor biotite and hornblende. Zircon, apatite, magnetite are common accessory minerals in the quartz monzodioritic and monzogranitic gneisses. Variable sericitization and chloritization of feldspar and hornblende are observed especially in some amphibolite and quartz monzodioritic gneiss samples (Fig. 4A and G).

4. Analytical methods

Whole-rock samples were trimmed to remove the weathered surfaces, and the fresh portions were chipped and powdered in an agate mill to about 200 mesh for major and trace element analysis. Sample powders were blended with lithium metaborate, and fused at 1100 ℃ in a Pt-Au crucible for 20-40 minutes. The melts were then cooled with resultant disks prepared for analysis. Loss on ignition (LOI) values were determined by measuring the weight loss after heating the samples at 1050 ℃ for 30 minutes. Major elements were analyzed using X-ray Fluorescence (XRF, Thermo Arl Advant XP+) at the Key Laboratory of Orogenic Belts and Crustal Evolution, Ministry of Education, Peking University, and were calibrated against standards GSR-15 (amphibolite), GSR-9 (diorite), and GSR-14 (granitoid gneiss). The analytical precision is ≤0.5% for major element oxides (Wang et al., 2012b; Bai et al., 2014a).

Sample powders for trace element analyses were pre-treated at Peking University. 25 mg of the powders were placed into Savillex teflon beakers, and then within a high-pressure bomb with a 1:1 mixture of HF-HNO_3. They were heated for 24 hours at 80℃, and then evaporated. After evaporation, 1.5 ml HNO_3, 1.5 ml HF and 0.5 ml $HClO_4$ were added, and the beakers were capped for digestion within a high-temperature oven at 180 ℃ for 48 hours or longer until the powders were completely digested. Finally, the residue was diluted with 1% HNO_3 to 50 ml. Trace elements, including rare earth elements (REEs), were measured using an ELEMENT-I plasma mass spectrometer (Finnigan-MAT Ltd.) at the Key Laboratory of Orogenic Belts and Crustal Evolution. Standards GSR-15, GSR-9, and GSR-14 were used for analytical control, and the measurement precision of trace elements was better than 5%.

Zircon grains were separated by standard density and magnetic techniques, and handpicked under a binocular microscope. These zircon grains were mounted in epoxy resin discs, and polished to half the grain thickness. Prior to analyses, cathodoluminescence images were obtained using a scanning electron microscope at the SEM Laboratory of Peking University. Then, they were analyzed for in-situ zircon U-Pb isotopes and trace elements using a laser ablation inductively coupled plasma mass spectrometer (LA-ICP-MS) at the Geological Lab Center, China University of Geosciences, Beijing (Yuan et al., 2004). During analyses, the laser spot diameter and frequency were 36 μm and 10 Hz, respectively. Harvard zircon 91500 was used as an external standard for zircon U-Th-Pb analyses, and NIST610 as an external standard to calculate the contents of U, Th, Pb, and other trace elements in the analyzed zircon grains. The $^{207}Pb/^{206}Pb$ and $^{206}Pb/^{238}U$ ratios were calculated using GLITTER program (van Achterbergh et al., 2001), and common Pb was corrected using the method of Anderson (2002). Age calculations and concordia plots were done using Isoplot (ver. 3.0) (Ludwig, 2003). Notably, it is common to have mixed analyses (i.e., down-hole variations) during LA-ICPMS U-Pb isotopic analyses because of intense laser ablation of the zircon grains. Nonetheless, these effects are insignificant for the chronological data in this study because of the following reasons. Firstly, the isotopic signals from the analyzed zircon spots show no apparent changes of the isotopic ratios for the 35-40 seconds' multiple analyses of any single zircon spot. Secondly, if heterogeneous domains of a zircon grain (e.g., magmatic core and metamorphic rim) were sampled, the dating results will show extremely large errors, possibly > 30 Ma (Condie et al., 2009). As shown by the data in the Supplementary Table 2, the majority of the analytical data have age errors of ≤ 30 Ma. Therefore, these chronological data can be used with confidence to constrain the sequences of geological events in the study region.

In-situ zircon Lu-Hf isotopic analyses were performed on the similar internal domains or close to the original pit used for U-Pb isotopic analyses, using a Neptune Plus MC-ICP-MS (Thermo Fisher Scientific, Gemany) attached to a Geolas 2005 excimer ArF laser ablation system (Lambda physik, Göttingen, Germany) at the state Key Laboratory of Geological Processes and Mineral Resources, China University of Geosciences in Wuhan (Hu et al., 2012). Beam diameter of 44 μm and repetition rate of 6 Hz were applied, and zircon 91500 and GJ-1 were used as the external standard and the unknown, respectively. During analyses, every eighth analysis of an unknown was followed by analyses of 91500 and GJ-1. The interference of ^{176}Yb and ^{176}Lu on ^{176}Hf could significantly affect the accuracy of ^{176}Hf/^{177}Hf ratios. ^{179}Hf/^{177}Hf and ^{173}Yb/^{171}Yb ratios were used to calculate the mass bias of Hf (β_{Hf}) and Yb (β_{Yb}), which were normalized to ^{179}Hf/^{177}Hf =0.7325 and ^{173}Yb/^{171}Yb=1.13017 (Segal et al., 2003) using an exponential correction for mass bias. Interference of ^{176}Yb on ^{176}Hf was corrected by measuring the interference-free ^{173}Yb isotope and using ^{176}Yb/^{173}Yb =0.79381 (Segal et al., 2003) to calculate ^{176}Yb/^{177}Hf. The relatively minor interference of ^{176}Lu on ^{176}Hf was corrected by measuring the intensity of the interference-free ^{175}Lu isotope and using the recommended ^{176}Lu/^{175}Lu =0.02656 (Blichert-Toft and Albarède, 1997) to calculate ^{176}Lu/^{177}Hf.

We used the mass bias of Yb (β_{Yb}) to calculate the mass fractionation of Lu because of their similar physicochemical properties. The determined $^{176}Hf/^{177}Hf$ ratios for standards 91500 (0.282290 ± 0.000022) and GJ-1 (0.282011 ± 0.000021) are within error of the reported values (Wu et al., 2006; Hu et al., 2012).

5. Results

5.1. Zircon U-Pb and Lu-Hf isotopes

Five representative samples, including two amphibolites (13PQ07-3 and 13PQ13-4), two dioritic gneisses (13PQ14-3 and 13PQ16-4), and one quartz monzodioritic gneiss (13PQ11-8), were analyzed for zircon U-Pb isotopes, with four of them (except for 13PQ07-3) analyzed for Lu-Hf isotopes (Supplementary tables 2-3). Rare earth element (REE) data of zircon grains for samples 13PQ07-3 and 13PQ13-4 are also analyzed and listed in Supplementary Table 4.

5.1.1. Zircon U-Pb isotopic dating data

5.1.1.1. Amphibolites: Sample 13PQ07-3 was collected in the Chagou area (N 41°06´24´´, E 118°16´11´´, Fig. 2). Zircon grains from this sample are small with lengths and length/width ratios of 80-120 μm and 1:1-2:1. CL images reveal mostly core-rim structures, with the banded or blurred oscillatory zoned or structureless cores enveloped by bright to dullish rims (Fig. 5A). Twenty-nine analyses were conducted on twenty-nine zircon grains, and except for spot #04, most plot on or close to the concordia with apparent $^{207}Pb/^{206}Pb$ ages of 2517 ± 25 to 1835 ± 30 Ma (Fig. 5B). They have Th and U contents ranging of 1-491 and 22-1570 ppm, yielding variable Th/U ratios of 0.03-1.83. On the chondrite-normalized REE plot (Supplementary Fig.

1A), most dated zircon grains show parallel and magmatic zircon-like REE patterns, i.e., positive Ce and negative Eu anomalies as well as steep HREE, suggesting their original crystallization from magmatic system (Supplementary Table 4; Rubatto, 2002). Some zircon grains show either higher light rare earth elements (LREEs) or lower total REE contents, possibly resulting from local element mobilization of the magmatic zircons (Whitehouse and Kamber, 2003). Four analyses on banded or blurred oscillatory zoned cores (#10, #11, #15, and #20) show the oldest apparent ages of 2517 ± 25 to 2496 ± 24 Ma with high Th/U ratios of 0.37-0.97. They yield a concordia age of 2503 ± 6 Ma (MSWD = 0.06) and a weighted mean age of 2501 ± 24 Ma (MSWD = 0.20), which are within error of each other. Their needle-shaped morphology, banded or oscillatory zoned internal structure, and high Th/U ratios (Fig. 5A), suggest that they are typical zircon grains crystallized from mafic magmas, but unlikely to be xenocrystic in origin (commonly eroded with subrounded shapes, Corfu et al., 2003). Therefore, the concordia age (2503 ± 6 Ma) calculated from this group of analyses (#10, #11, #15, and #20) can be taken as the best estimate of the crystallization age of the basaltic precursors. Notably, the host metabasaltic rock has moderate MgO (5.86 wt.%) and Mg# (46.81, 100Mg/(Mg+Fe_{total}) atomic ratio) (Supplementary Table 1), suggesting that the magmatic zircon grains in this sample were crystallized from an evolved basaltic magma system. Except for the above four analyses, the other analyses were performed on dark cores or bright structureless domains with Th/U ratios ranging of 0.03-1.83, and they yield four younger age clusters: (1) nine analyses with apparent ages of 2493 ± 25 to 2457 ± 24 Ma give an upper intercept age of 2468 ± 9 Ma (MSWD = 1.5), with the eight concordant analyses (except spot #04) yielding a weighted mean age of 2467 ± 17 Ma (MSWD = 0.25); (2) three analyses with ages of 2423 ± 27 to 2380 ± 26 Ma give a weighted mean age of 2402 ± 30 Ma (MSWD = 0.65); (3) eleven analyses with ages of 2176 ± 27 to 2065 ± 27 Ma; and (4) two analyses of bright structureless domains yield the youngest ages of 1845 ± 29 and 1835 ± 30 Ma. These younger ages are inferred to reflect effects of multiple Paleoproterozoic tectonothermal events (Liu et al., 2007a, 2011a; Wang et al., 2015b).

Zircon grains from sample 13PQ13-4 collected in the vicinity of Qigou (N 40°58´40´´, E 118°20´59´´, Fig. 2) are small, with lengths and length/width ratios of 80-150 μm and 1:1-2:1, respectively, and display mostly core-rim structures on the CL images (Fig. 5C). Some cores show needle-like shapes and banded zoning (e.g., #3 and #10), whereas others are bright or dark structureless, and all are surrounded by dullish structureless rims. Thirty analyses conducted on thirty grains give apparent $^{207}Pb/^{206}Pb$ ages of 2609 ± 25 to 2361 ± 23 Ma, and Th and U contents of 38-626 and 49-1505 ppm, respectively, with Th/U ratios of 0.27-1.28. On the chondrite-normalized REE plot (Supplementary Fig. 1B), most dated spots show parallel and magmatic zircon-like REE patterns, i.e., positive Ce and negative Eu anomalies as well as steep HREE, suggesting their original crystallization from magmatic system (Supplementary Table 4; Rubatto, 2002). Some zircon grains (e.g., #02 and #03) show higher contents of LREE, possibly resulting from local element mobilization of the magmatic zircons (Whitehouse and Kamber, 2003). Spot #29 is an analysis of a bright structureless core with a rounded shape, and its age of 2609 ± 25 Ma is much older than the main age mode, and is considered to be a xenocrystic grain (Fig. 5D). Six analyses on banded or blurred zoned cores show ages of 2519 ± 24 to 2502 ± 23 Ma, yielding a concordia age of 2506 ± 5 Ma (MSWD = 0.31) and a weighted mean age of 2508 ± 19 Ma (MSWD = 0.09). Considering their needle-shaped morphology, magmatic-like internal structures, and high Th/U ratios (0.87-1.05), these six grains likely have been crystallized from a basaltic magma system, but not xenocrystic in origin (Corfu et al., 2003). Therefore, the age of 2506 ± 5 Ma is considered to be close to the crystallization age of the magmatic precursor. Nineteen analyses on dark or bright structureless cores with ages of mostly 2493 ± 24 to 2481 ± 23 Ma define a discordia, yielding an upper intercept age of 2488 ± 9 Ma (MSWD = 0.15). Three analyses (#05, #25, and #28) on bright structureless cores show ages of 2461 ± 24 to 2442 ± 23 Ma, with a weighted mean age of 2452 ± 27 Ma (MSWD = 0.16). Spot #19 on a dark core gives the youngest age of 2361 ± 23 Ma. Ages younger than the crystallization age are taken to reflect regional Paleoproterozoic tectonothermal events (Liu et al., 2011a; Wang et al., 2015b).

5.1.1.2. Dioritic gneisses: Sample 13PQ14-3 (N 41°06´54´´, E 118°21´34´´) was collected in the Shidaohe area (Fig. 2). Zircon grains are larger than those from the amphibolites, being 200-250 μm in length with length/width ratios of 1:1-1.5:1 (Fig. 6A). Cathodoluminescence images reveal variably eroded oscillatory zoned or dark structureless cores that are enveloped by bright to dullish rims. Thirty analyses were conducted on thirty zircon grains, which all plot on concordia with apparent $^{207}Pb/^{206}Pb$ ages of 2543 ± 15 to 2424 ± 13 Ma (Fig. 6B). Th and U contents range from 24-239 and 59-653 ppm, respectively, yielding high Th/U ratios of 0.33-0.83. Twelve older analyses (2543 ± 15 Ma to 2501 ± 13 Ma) mainly on the oscillatory zoned cores yield a concordia age of 2515 ± 4 Ma (MSWD < 0.01) and a weighted mean age of 2516 ± 7 Ma (MSWD = 1.06), and the former age is taken as the crystallization age of the dioritic magmatic precursor. Twelve analyses of dark structureless cores or rims show younger apparent ages of 2497 ± 11 to 2470 ± 12 Ma, yielding a concordia age of 2485 ± 4 Ma (MSWD = 0.01) and a weighted mean age of 2486 ± 7 Ma (MSWD = 0.78). Six analyses on structureless cores or bright rims give the youngest apparent ages of 2455 ± 12 to 2424 ± 13 Ma. These younger ages are considered as the effects of Paleoproterozoic tectonothermal events, which are not only recorded in the nearby Dantazi Complex, but also well documented along the entire northwestern margin of the Eastern Block (Liu et al., 2007a,b, 2011a,b; Wang et al., 2015b).

Zircon grains from sample 13PQ16-4 (Qigou area; N 41°00´21´´, E 118°25´37´´, Fig. 2) have lengths of 150-200 μm and length/width ratios of 1:1-1.5:1. On CL images, most grains show core-rim structures, with prismatic or eroded oscillatory zoned cores surrounded by bright rims, with some cores almost completely consumed by recrystallization (Fig. 6C). Twenty-five analyses were conducted on twenty-five zircon grains, and most plot on concordia with apparent $^{207}Pb/^{206}Pb$ ages of 2561 ± 18 to 2298 ± 19 Ma, except for spot #12 falling below the concordia possibly due to Pb loss (Fig. 6D). They have Th and U contents of 29-572 and 122-828 ppm, with Th/U ratios of 0.20-0.80. Twenty analyses on oscillatory zoned cores with ages of 2561 ± 18 - 2501 ± 16 Ma yield a concordia age of 2537 ± 4 Ma (MSWD = 0.02) and a weighted mean age of 2538 ± 7 Ma (MSWD = 0.56). Four analyses on bright structureless rims (#3, #10, #14, and #18) give younger ages of 2497 ± 17 to 2298 ± 19 Ma, and a weighted mean age of 2478 ± 18 Ma (MSWD = 0.87) is obtained from the first three spots. Based on the zircon internal structures, the magmatic precursor is considered to have been emplaced at 2537 ± 4 Ma, and subjected to later ~2478 and ~2298 Ma metamorphism.

5.1.1.3. Quartz monzodioritic gneiss: Sample 13PQ11-8 is from Shidaohe area (N 41°07´05´´, E 118°19´29´´, Fig. 2). Zircon grains have oval to stubby shapes with lengths and length/width ratios of 150-220 μm and 1:1-1.5:1. CL images reveal oscillatory zoned or bright to dark structureless cores that are enveloped by thin dullish structureless rims (Fig. 7A). Twenty-five analyses conducted on twenty-five zircon grains all plot on the concordia with apparent $^{207}Pb/^{206}Pb$ ages of 2495 ± 11 to 2371 ± 15 Ma (Fig. 7B). Th and U contents vary of 12-169 and 19-273 ppm with Th/U ratios of 0.32-0.94. Four analyses of oscillatory zoned cores show the oldest apparent ages of 2495 ± 11 to 2487 ± 11 Ma, yielding a concordia age of 2491 ± 6 Ma (MSWD < 0.01) and a weighted mean age of 2492 ± 12 Ma (MSWD = 0.10), within error of each other. Thirteen analyses of bright or dark structureless cores give younger ages of 2465 ± 11 to 2421 ± 13 Ma, yielding a weighted mean age of 2447 ± 6 Ma (MSWD = 0.95). Other eight analyses of bright structureless domains show the youngest ages of 2414 ± 13 to 2371 ± 15 Ma, with a weighted mean age of 2395 ± 12 Ma (MSWD = 1.3). On the basis of zircon internal structures, the magmatic precursor was emplaced at 2491 ± 6 Ma, and then subjected to later ~2447 Ma and ~2395 Ma tectonothermal events that are prevalent in the Northern Hebei Province as well as the northwestern margin of the Eastern Block (Liu et al., 2007a,b, 2011a,b; Wang et al., 2015b).

5.1.2. Zircon Lu-Hf isotopes

Twenty dated zircon spots from each sample were analyzed for Lu-Hf isotopes (Supplementary Table 3). Calculated at the apparent $^{207}Pb/^{206}Pb$ ages (t_1), most analyses for each sample yield nearly consistent $^{176}Hf/^{177}Hf(t_1)$ ratios: 0.281221-0.281334 for sample

13PQ13-4, 0.281173-0.281292 for sample 13PQ14-3, 0.281146-0.281268 for sample 13PQ16-4, and 0.281207-0.281307 for sample 13PQ11-8 (Fig. 8A, C, E, and G). This implies that except for the xenocrystic zircon grain (13PQ13-4-01), all other igneous grains from each of the four samples crystallized from the same magmatic system but were subjected to different degrees of subsequent Pb loss (Zeh et al., 2007). Furthermore, the age of 2506 Ma calculated from the oldest age group of amphibolite sample 13PQ13-4 could represent the best estimate for the crystallization age. Two younger analyses of sample 13PQ16-4 give higher $^{176}Hf/^{177}Hf(t_1)$ values of 0.281324 and 0.281289 (#02 and #15). Their Lu-Hf isotopic system may have been reset by later high-grade metamorphism, and are rejected from further calculation. When calculated at the crystallization ages (t_2), these samples yield almost positive $\varepsilon Hf(t_2)$ values of +1.4 to +5.4 (13PQ13-4), -0.1 to +4.1 (13PQ14-3), -0.6 to +3.8 (13PQ16-4), and +0.5 to +4.1 (13PQ11-8) (Fig. 8B, D, F, and H). The xenocrystic spot 13PQ13-4-01 gives a positive value of +6.4. Notably, the highest $\varepsilon Hf(t_2)$ values of each sample are lower than that of depleted mantle but close to the "New Crust" evolution line calculated from the juvenile crust generated in modern island arcs worldwide (Dhuime et al., 2011).

5.2. Whole-rock geochemistry

For comprehensive understanding of Archean crust-mantle interactions of the Northern Hebei Province, the Pingquan samples are integrated with published data for metabasalts from Dantazi Complex, and dioritic/TTG gneisses from both Dantazi and Huai'an-Xuanhua complexes (Supplementary Table 1 and Figs. 9-10).

The Pingquan amphibolite samples and metabasaltic rock samples from Dantazi

Complex show SiO_2 contents of mostly 48.45-53.19 wt.% and MgO of 3.06-13.23 wt.%. In the Zr/TiO_2*0.0001 vs. Nb/Y diagram, they all plot in the basaltic field and belong to calc-alkaline rock series in the La-Yb binary diagram (Fig. 9A-B). Most of them have Fe_2O_3T and TiO_2 of 9.35-14.06 wt.% and 0.52-1.92 wt.%, whereas samples GB30 and GB33 exhibit lower SiO_2 (43.60-44.30 wt.%) but higher Fe_2O_3T and TiO_2 of 18.47-18.60 wt.% and 3.49-3.51 wt.%. Parental magmas for these two samples may have experienced accumulation of Fe-Ti oxides, which can explain their relatively lower silica contents (Ge et al., 2015). Their Mg# values ($100Mg/(Mg+Fe_{total})$ atomic ratio) vary widely from 33.51 to 68.40. They have parallel and moderately fractionated chondrite-normalized REE patterns (Fig. 10A), with $(La/Sm)_N$ and $(La/Yb)_N$ ratios of 1.98-4.22 and 5.50-21.75 as well as weakly negative to positive Eu anomalies (Eu_N/Eu_N^*=0.75-1.18). Sample 13PQ13-4 has a higher total content of rare earth elements (TREE of 477 ppm vs. 82-269 ppm). On the primitive mantle-normalized diagram (Fig. 10B), most of them show negative Nb, Ta, and Ti anomalies with low $(Nb/La)_{PM}$ ratios of 0.15-0.48. Positive Ti anomalies of samples GB30 and GB33 could have resulted from the accumulation of Fe-Ti oxides (Ge et al., 2015).

The dioritic and TTG gneisses have SiO_2 contents from 52.86 to 72.10 wt.%, and they all belong to the calc-alkaline rock series in the total alkalis-silica (TAS) diagram (Middlemost, 1994; Fig. 9C-D). Dioritic gneisses show SiO_2 contents of 52.86-61.02 wt.%, MgO of 2.75-6.56 wt.% (mostly >3.68 wt.%) and Fe_2O_3T of 6.27-12.63 wt.%, with Mg# values of 41.23-56.95. In the MgO vs. SiO_2 diagram (Fig. 9E), most samples plot in the field of low-silica adakite (LSA; Martin et al., 2005). They display high Na_2O of 2.43-5.26 wt.% but low K_2O/Na_2O ratios of 0.22-0.71. The CaO and Al_2O_3 contents vary of 3.89-8.88 and 12.73-19.88 wt.% (mostly of

14.46-17.61 wt.%), with A/CNK values (molar $Al_2O_3/(CaO+Na_2O+K_2O)$) of 0.74-1.06 (mostly of 0.74-0.90), and TiO_2 and P_2O_5 range of 0.51-0.95 and 0.11-0.40 wt.%, respectively. In the chondrite-normalized REE diagram (Fig. 10C), dioritic gneisses are moderately fractionated with $(La/Sm)_N$ and $(La/Yb)_N$ ratios of 1.84-5.39 and 5.26-23.05, as well as dominantly negative Eu anomalies (Eu_N/Eu_N^* of 0.57-1.28 (mostly <0.95)). In the primitive mantle-normalized multi-element diagram (Fig. 10D), they are enriched in Rb, Ba, K, Zr and Hf, but depleted in Nb, Ta, Ti, and Th, and featured by moderate to high Yb and Y contents of 1.23-2.22 and 13.53-25.67 ppm with Sr/Y ratios of 14.49-64.28.

TTG gneiss samples of the Northern Hebei Province plot chiefly in the tonalite and granodiorite fields in the An-Ab-Or diagram (Fig. 9D; O'Connor, 1965), with Na_2O contents (3.39-6.36 wt.%) and K_2O/Na_2O ratios (0.17-0.79) comparable with those of dioritic gneisses. They have Al_2O_3 contents of 14.73-17.77 wt.%, and moderate to high A/CNK values of 0.76-1.14. In spite of this, the TTG gneisses are characterized by chemical features apparently distinct from the dioritic gneisses: (1) higher SiO_2 (62.40-72.10 wt.%), but lower MgO (0.55-3.72 wt.%) and Fe_2O_3T (1.87-7.01 wt.%) contents, with Mg# values of 32.67-57.58; in the MgO vs. SiO_2 diagram (Fig. 9E), most TTG gneisses fall in the field of experimentally-derived partial melts from metabasalts, with some gneisses of lower silica contents (63.02-65.54 wt.%) falling in the high-silica adakite (HSA) field (Martin et al., 2005); (2) lower CaO (2.44-5.78 wt.%), TiO_2 (0.11-0.60 wt.%) and P_2O_5 (0.04-0.21 wt.%) contents; (3) strongly fractionated chondrite-normalized REE patterns (Fig. 10C), with higher $(La/Sm)_N$ and $(La/Yb)_N$ ratios of 2.11-10.54 and 10.09-56.78, and mostly positive Eu anomalies (Eu_N/Eu_N^* = 0.80-3.41); and (4) enrichment in Rb, Ba, K, Zr and Hf, but depletion in Nb, Ta, Ti, and Th in the primitive mantle-normalized multi-element diagram (Fig. 10D), with lower Yb (0.14-1.03 ppm) and Y (2.86-12.05 ppm) contents and higher Sr/Y ratios (48.31-260.62).

The quartz monzodioritic and monzogranitic gneiss samples have SiO_2 contents of 57.45-75.17 wt.%, and MgO contents and Mg# values of 0.02-2.54 wt.% and 3.20-45.32. In the An-Ab-Or diagram (Fig. 9D), they plot in the granodioritic to granitic fields, with high K_2O contents of 2.70-6.27 wt.% and K_2O/Na_2O ratios of 0.89-2.45, different from those of dioritic and TTG gneisses. On the MgO vs. SiO_2 diagram (Fig. 9E), all of them fall into the field of experimentally derived partial melts from metabasalts (Martin et al., 2005). They are weakly to strongly peraluminous (A/CNK values of 0.99-1.23), despite variable Al_2O_3 contents of 13.52-19.77 wt.%. In the chondrite-normalized REE diagram (Fig. 10E), the samples show moderately fractionated patterns, and most of them have TREE contents of 105-221 ppm, $(La/Sm)_N$ and $(La/Yb)_N$ ratios of 3.59-6.36 and 11.94-30.73, with weakly negative to evidently positive Eu anomalies (Eu_N/Eu_N^* = 0.72-1.88). The most felsic sample 13PQ17-1 (SiO_2 content of 75.17 wt.%) has the lowest TREE content of 41 ppm, showing the most positive Eu anomaly (Eu_N/Eu_N^* = 1.90) and a flat heavy rare earth element (HREE) pattern ($(Gd/Yb)_N$ value of 1.72; Fig. 10E). In the primitive mantle-normalized multi-element diagram (Fig. 10F), they are depleted in Nb, Ta, and Ti, but enriched in Zr and Hf, with highly variable Th contents. Most of them have Y and Yb contents of 8.90-20.20 and 0.73-1.94 ppm, with Sr/Y ratios of 18.58-77.78. Sample 13PQ17-1 has an evidently negative Sr anomaly, with lower Y and Yb contents of 3.30 and 0.38 ppm, and a lower Sr/Y ratio of 10.67 (Fig. 10F).

6. Discussion

6.1. Chronological framework of the Northern Hebei Province

Zircon U-Pb isotopic age data reveal that the Pingquan Complex experienced three magmatic episodes, generating ~2537-2515 Ma diorites, ~2506-2503 Ma basalts, and ~2491 Ma quartz monzodioritic to monzogranitic rocks (Figs. 5-7). These rocks were subjected to regional metamorphism at ~2480 Ma (2488 ± 9 - 2467 ± 17 Ma), whereas ~2455-2395 Ma metamorphic ages are variably recorded. These early Paleoproterozoic metamorphic events are common along the northern margin of Eastern Block and some neighbouring Neoarchean complexes in the TNCO, e.g., ~2485 Ma granulite facies followed by ~2450 Ma and ~2401 Ma retrograde metamorphism in the adjacent Western Liaoning Province (Liu et al., 2007a, 2011a; Wang et al., 2011, 2013, 2015b). Younger metamorphic ages of ~2361-2298 Ma, ~2176-2065 Ma and ~1845-1835 Ma imply that the Pingquan Complex was also subjected to the effects of the middle to late Paleoproterozoic orogenesis that affected the TNCO (Zhao et al., 1998, 2005, 2012; Guo et al., 2002, 2005; Yang and Santosh, 2015).

Recent zircon U-Pb isotopic dating data for the NHB are compiled in Supplementary Table 5, with major early Precambrian tectonothermal events summarized as follows (Fig. 11): (a) traces of xenocrystic zircon grains with ages of mostly 2636 ± 30 - 2565 ± 16 Ma (only one age of 2799 ± 23 Ma) possibly imply some cryptic ~2600-2560 Ma metavolcanic rocks but no record of substantial early Neoarchean (~2.7 Ga) or older geological records (Liu et al., 2007a); (b) ~2542-2499 Ma dioritic and TTG gneisses are the dominant lithologies in NHB, followed by eruption of basaltic rocks with minor andesitic to rhyolitic rocks at ~2506-2502 Ma in the Pingquan and Dantazi complexes; (c) subsequently, quartz monzodioritic and syeno-/monzogranitic rocks were emplaced at ~2493-2484 Ma; and (d) the basement rocks of

NHB witnessed multiple episodes of early and late Paleoproterozoic metamorphism (early peaks at ~2480, ~2450, and ~2400 Ma, and a late peak at ~1850 Ma). Notably, early Paleoproterozoic metamorphic imprints are respectively synchronous with (1) ~2496-2484 Ma potassium-rich magmatism along the northern margin of EB as well as some quartz dioritic magmatism in Northern Liaoning; (2) ~2454-2437 Ma charnockitic to granitic magmatism in Huai'an-Xuanhua Complex; and (3) ~2410 Ma granitic magmatism in Huai'an-Xuanhua Complex and ~2403-2399 Ma quartz dioritic and gabbroic magmatism in Western Liaoning (Liu et al., 2010; Zhang et al., 2011; Wan et al., 2012; Bai et al., 2014b; Wang et al., 2015b; Yang and Santosh, 2015). Whereas late Paleoproterozoic metamorphic ages reflect the effects of final amalgamation of the EB and WB along the TNCO at ~1.85 Ga, and are coeval with ~1859-1849 Ma mafic to felsic magmatism in Northern Hebei Province (Fig. 11A; Zhao et al., 2005, 2008, 2012; Liu et al., 2007a,b). Combined with minor ~2300-1900 Ma metamorphic imprints and magmatic events (Fig. 11B), we consider that Neoarchean basement rocks of Northern Hebei Province were involved in both early Paleoproterozoic arc-continent accretion along northwestern EB and middle to late Paleoproterozoic subduction-collision processes of the TNCO (Fig. 1; Zhao et al., 2012; Wang et al., 2015b).

6.2. Petrogenesis

6.2.1. Assessment of element mobility

Considering the evidence for multiple episodes of metamorphism in the study area (Figs. 4 and 11), element mobility should be evaluated prior to any petrogenetic discussions. Firstly, most samples have low loss on ignition (LOI) values of 0.32-4.43 wt.%, apart from amphibolite sample 13PQ14-12 with a higher value of 7.34 wt.%. Secondly, each group of samples exhibits nearly parallel normalized REE and high field strength element (HFSE; e.g., Nb, Ta, Zr, and Hf) patterns (Fig. 10), implying the preservation of original compositions of these elements. Lower contents of heavy rare earth elements of TTG gneisses relative to dioritic gneisses (Fig. 10C) can be ascribed to diverse genetic processes that will be discussed below. However, large variations of Ba, Rb, and Th suggest mobility of these elements. Thirdly, negligible Ce anomalies ($Ce_N/Sqrt(La_N \times Pr_N)$ ratios of mostly 0.96-1.06, and only sample 13PQ17-1 with a lower value of 0.87) are consistent with those of unaltered samples (0.9-1.1; Polat and Hofmann, 2003). Finally, La, Sm, and Nb show nearly linear correlations with alteration-insensitive Zr for each sample group, whereas Th, Rb, and Ba vary widely (Supplementary Fig. 2). Accordingly, the petrogenetic and other discussions below will rely dominantly on MgO, Al_2O_3, TiO_2, REEs, HFSEs, and transition metals that are commonly viewed as immobile under high grade metamorphism (Guo et al., 2013, 2015a; Pearce, 2014).

6.2.2. Metabasaltic rocks (Pingquan amphibolites and metabasalts of Dantazi Complex)

Metabasaltic rocks of the NHB show variable major element contents but parallel chondrite-normalized REE patterns (Supplementary Table 1 and Fig. 10A). The positive zircon $\varepsilon Hf(t_2)$ values (Pingquan amphibolites: +1.4 - +5.4; Dantazi metabasalts: mostly +1.3 - +4.4) are lower than that of depleted mantle (Fig. 8B; Ge et al., 2015). The above data suggest that their parental magmas may have experienced certain degrees of crustal contamination and/or fractional crystallization. On the La/Sm vs. La diagram (Fig. 12A), most samples define a roughly horizontal line reflecting effects of fractional crystallization (Treuil and Joron, 1975; Liu et al., 2012a). With elevated silica contents, they display a decrease in CaO/Al_2O_3 ratios (Fig. 12B), together with less variable Fe_2O_3T with decreasing TiO_2 and V contents (Fig. 12C), indicating clinopyroxene and hornblende fractionation (but no plagioclase and Fe-Ti oxides; Rollinson, 1993). In spite of this, the lack of negative correlation between $(Nb/La)_{PM}$ and $(La/Sm)_N$ and consistently lower $(Nb/La)_{PM}$ ratios (0.15-0.32) argue against significant crustal contamination for the mantle-derived parental magmas. This is further evidenced by the general lack of xenocrystic zircons (Fig. 5), with only one zircon grain (2609 ± 25 Ma) coeval with regional ~2640-2603 Ma MORB-like tholeiites in Western Liaoning (Wang et al., 2015b). Samples GB30 and GB33 display Fe-Ti enrichment and accumulation of Fe-Ti oxides, and these imply an oxidized parental magma that could not be consanguineous with other samples, as reflected by lower La/Sm but higher $(Nb/La)_{PM}$ ratios and Zr, Nb, and P contents (Fig. 12A-D; Ge et al., 2015). Accordingly, these metabasaltic rocks should have been derived from a moderately depleted mantle but without participation of crustal contamination, i.e., the isotopic and other geochemical features excepting the mobile Ba, Rb and Th reflect essentially the nature of the mantle source region and magmatic processes.

Compared to N-MORBs, these metabasaltic samples have lower Zr/Nb (5.77-21.94 vs. 31.76) and Hf/Nb (0.18-0.64 vs. 0.88) but higher Nb/Yb (2.05-6.61 vs. 0.76) and Zr/Yb (27.81-112.82 vs. 24.26) ratios, resembling those of enriched MORBs (Fig. 12E; Sun and McDonough, 1989; Pearce and Peate, 1995). Mantle enrichment can be achieved by crustal recycling at convergent margins or mantle overturn/plume events (Dhuime et al., 2011; Kamber, 2015; Rollinson, 2015). Imprints of Neoarchean mantle overturn/plume events were not identified along northwestern EB, e.g., komatiites, tholeiitic to alkaline basalts, and layered mafic-ultramafic intrusions (Liu et al., 2011a; Nutman et al., 2011; Bai et al., 2014a, 2015; Wang et al., 2015b, 2016). Carbonatite metasomatism can also be precluded based on chondrite-like Zr/Hf ratios (mostly 32.88-40.29) and lack of positive correlation between Nb/Ta and Lu-Hf ratios (not shown, Dupuy et al., 1992; Pfänder et al., 2012; Wang et al., 2015c). Therefore, the moderately depleted mantle sources for these metabasaltic rocks likely resulted from crustal recycling at a subduction zone, compatible with the arc-like trace element patterns (Fig. 10B). Sediment recycling has contributed to mantle heterogeneity and geochemical complexity of arc lavas at subduction zones (Woodhead et al., 2001; Handley et al., 2011; Rollinson, 2015). Notably, TTG gneisses in Huai'an-Xuanhua Complex show zircon εHf(t) (+2.3 - +8.2) and whole-rock εNd(t) values (+2.5 - +4.3) close to those of depleted mantle, and were considered to have been derived from partial melting of subducted slabs (Liu et al., 2009, 2012b). This implies that isotopically enriched materials (i.e., oceanic sediments) could have been recycled so as to form the moderately depleted mantle sources (Fig. 8B). Subducted sediments exhibit diverse geochemical features (i.e., zircon effects): detrital-rich turbidites show lower Sm/Hf ratios and εHf(t) values than those of clay-rich pelagic sediments (Carpentier et al., 2009). Though clinopyroxene or hornblende fractionation ($D_{Sm/Hf}$>1) may decrease Sm/Hf ratios of arc lavas, these metabasaltic rocks display high Sm/Hf ratios (1.59-2.55) (Fig. 12F). Coupled with lower $(^{176}Hf/^{177}Hf)_{initial}$ ratios relative to those of ~2.5 Ga depleted MORB mantle (calculated from Chauvel and Blichert-Toft (2001)), metabasaltic rocks in the NHB could have been derived from a lithospheric mantle metasomatized by pelagic sediments, and experienced some clinopyroxene and hornblende fractionation (Handley et al., 2011).

6.2.3. Dioritic and TTG gneisses

Both the Huai'an-Xuanhua dioritic and TTG gneisses were previously considered to be generated by partial melting of oceanic slabs with melts contaminated by the mantle wedge (Liu et al., 2012b). High Na_2O contents, low K_2O/Na_2O ratios, moderate to high MgO and Mg# values, and strongly fractionated chondrite-normalized REE patterns of the TTG gneisses are indeed analogous to those of high-silica adakites (Figs. 9D-E and 10C; Martin et al., 2005; Wang et al., 2013). In contrast, integrated with samples from Pingquan and Dantazi complexes, dioritic gneisses of the NHB exhibit contrasting geochemical features to those of TTG gneisses, including: (1) higher TiO_2 and Nb contents (0.51-0.95 vs. 0.11-0.60 wt.% and 2.36-9.71 (half samples >6.10) vs. 1.31-5.86 ppm); (2) lower $(La/Yb)_N$ and higher Yb and Y contents resembling Phanerozoic arc basaltic-andesitic-dacitic-rhyolitic rocks (Fig. 13A); and (3) lower whole-rock εNd(t) values (+0.8-+1.7 vs. +2.5-+4.3) (Liu et al., 2009). On the La/Sm vs. La diagram (Fig. 13B), dioritic gneisses define a horizontal line that is an indicator of petrogenetic processes controlled by fractional crystallization, which deviates from the roughly positive slope line of TTG gneisses. Samples 05LF04, 05LF52, and JB050-1 possess high La/Sm, low La and positive Eu anomalies ($Eu_N/Eu_N^* = 1.79\text{-}3.41$), possibly caused by plagioclase accumulation ($D_{La}(Pl)<1$; $D_{La/Sm}(Pl)>1$; Rollinson, 1993). Comparable Gd/Yb ratios suggest that the TTG magmas could not have been derived from hornblende fractionation from a dioritic magma (Fig. 13C; Rollinson, 1993; Wang et al., 2015b). In fact, dioritic gneisses have low SiO_2 (low to 52.86 wt.%) and high MgO contents (up to 6.56 wt.%) analogous to those of high magnesian andesites (HMAs), suggesting derivation from a mantle source (Fig. 9D; Kelemen et al., 2004; Tatsumi, 2006). Specifically, the adakite-like model was assigned to the dioritic gneisses based mainly on low TiO_2 contents (0.51-0.95 wt.%), just like low-Ti sanukitoids (<1.0 wt.%; Liu et al., 2012b). Nevertheless, Phanerozoic primitive HMAs show TiO_2 contents of mostly <1.0 wt.% (Grove et al., 2012), and low-Ti sanukitoids may also be formed by high degree partial melting of a mantle source (with low degree of metasomatism; Martin et al., 2010). Therefore, parental magmas of dioritic gneisses in this study likely have been derived from a metasomatized mantle source, and a single slab-melting model cannot explain the geochemical discrepancies between dioritic and TTG gneisses (Martin et al., 2005; Wang et al., 2012a, 2016). In other words, the dioritic magmas should have originated from a different source region from those of TTG magmas, and may be derived from either partial melting of a depleted mantle source metasomatized by slab fluids/melts or fractional crystallization of the basaltic magmas that formed metabasaltic rocks in the NHB.

The dioritic gneisses show variable major element compositions (e.g., SiO_2 and MgO; Supplementary Table 1), and these can be explained by clinopyroxene fractionation based on positive correlation between CaO/Al_2O_3 ratios and MgO contents (Fig. 13D). Weakly positive to negative Eu anomalies (Eu_N/Eu_N^*=0.57-1.28) suggest some plagioclase fractionation (Fig. 10C). Although moderately depleted zircon $\varepsilon Hf(t_2)$ values of the Pingquan dioritic gneisses (Fig. 8C and E), significant crustal contamination can be precluded by the absence of xenocrystic zircon grains (Fig. 6) as well as consistently low $(Nb/La)_{PM}$ ratios (mostly of 0.11-0.39; only sample 05LF51 shows a higher value of 0.55; Fig. 13E). In comparison, the Huai'an-Xuanhua dioritic gneisses have high zircon $\varepsilon Hf(t_2)$ values close to those of depleted mantle (Liu et al., 2009), but decoupled from the moderately depleted whole-rock $\varepsilon Nd(t)$ values (+0.8-+1.7) (note that parallel normalized REE patterns in Fig. 10C imply general preservation of original Sm, Nd contents and εNd(t) values). Similar Hf-Nd decoupling has been well established in island arc lavas and ocean-island basalts, indicating recycling of “zircon-free” pelagic sediments into the mantle sources (Nebel et al., 2011). Therefore, similar to the metabasaltic rocks, these dioritic gneisses could also have been derived from a moderately depleted lithospheric mantle metasomatized by melts from recycled pelagic sediments (Figs. 8 and 12E-F). This is further evidenced from moderate to high Sm/Hf (mostly of 1.15-2.47) and low ($^{176}Hf/^{177}Hf)_i$ ratios (Fig. 13F; Handley et al., 2011). Lower Sm/Hf ratio of sample 13PQ16-4 is better ascribed to clinopyroxene fractionation as discussed above (Fig. 13D).

6.2.4. Quartz monzodioritic and monzogranitic gneisses

Archean K-rich granitoid gneisses are commonly considered to be derived from partial melting of either metasomatized lithospheric mantle (sanukitoid series) or crustal materials (granodioritic-monzogranitic series), though asthenospheric mantle may be involved in some Fe-K granitoid gneisses (Moyen et al., 2003; Martin et al., 2005; Laurent et al., 2014a). Quartz monzodioritic gneisses in the Pingquan Complex are characterized by low SiO_2, high K_2O and ferromagnesian oxides (FeO_T + MgO + MnO + TiO_2 = 6.80-8.97 wt.%), as well as moderately fractionated chondrite-normalized REE patterns (Figs. 9D-E and 10E). These features resemble those of sanukitoid rocks or Closepet-type granites, despite slightly lower MgO and Mg# values (Fig. 14A; Heilimo et al., 2013). Entrainment of peritectic clinopyroxene/garnet may explain geochemical diversity and high maficity (maficity = atomic (Fe+Mg) per 100 g rock) of crust-derived granitoids (Clemens and Stevens, 2012). Nevertheless, the lack of correlation between A/CNK values (0.99-1.20) and maficity (0.02-0.14) and low SiO_2 contents suggest that the quartz monzodioritic gneisses cannot be formed solely by crustal reworking (Fig. 14B; Rapp and Watson, 1995). With increasing SiO_2 contents, they show constant or increasing Fe_2O_3T, TiO_2, and P_2O_5 contents (Supplementary Table 1), together with the paucity of regionally coeval (~2491 Ma) mafic rocks, precluding magma mixing as a viable genetic model (Nutman et al., 2011; Wang et al., 2016). Crustal contamination is also unlikely since no xenocrystic zircon grains are detected in the dated sample (Fig. 7) as well as similarly low $(Nb/La)_{PM}$ (0.12-0.33) at variable $(La/Sm)_N$ ratios (3.59-6.36). Furthermore, these samples have higher Al_2O_3 (>15.84 vs. <15 wt.%) and lower FeO_T (4.54-6.04 vs. >7 wt.% at ~60 wt.% silica) that are distinct from those of late Archean Matok Fe-K granitoids (South Africa) with imprints of asthenospheric mantle (Laurent et al., 2014a). Accordingly, magmatic precursors of these quartz monzodioritic gneisses were likely derived from a metasomatized lithospheric mantle source. Dated sample 13PQ11-8 shows a moderately depleted zircon $\varepsilon Hf(t_2)$ values (+0.5 - +4.1) (Fig. 8H), with initial $^{176}Hf/^{177}Hf$ values lower than those of depleted mantle (Fig. 14C). Notably, the quartz monzodioritic gneisses are clearly differentiated relative to primitive sanukitoid melts (Fig. 9D; MgO > 6 wt.% and Mg# > 60; Laurent et al., 2013), which can explain the large scatter of Sm/Hf ratios (0.53-2.27). Considering mostly peraluminous features (A/CNK = 0.99-1.20) and comparable zircon Lu-Hf isotopic compositions to metabasaltic rocks and dioritic gneisses (Figs. 8 and 14B), a similar lithospheric mantle source with recycled pelagic sediments is favored for these quartz monzodioritic gneisses.

Compared to quartz monzodioritic gneisses, monzogranitic gneisses display higher SiO_2 and K_2O contents and lower ferromagnesian oxides (FeO_T + MgO + MnO + TiO_2 = 1.25-6.48 wt.%), marking probable derivation from crustal materials without significant involvement of mantle components (Fig. 9D; Martin et al., 2005; Wan et al., 2012). Low Zr and V contents (64-279 and 10.3-62 ppm) also resemble those of crust-derived late Archean biotite granites (Laurent et al., 2014b). Generation of monzogranitic rocks by hornblende fractionation from a quartz monzodioritic magma was unlikely, due to roughly comparable Gd/Yb ratios (Fig. 14D). Synchronous Huai'an-Xuanhua granitic rocks show moderately depleted zircon εHf(t) values of +1.3 - +5.8, indicating derivation from a juvenile crustal source (Zhang et al., 2011). In the AFM (molar $Al_2O_3/(FeO_T+MgO)$) vs. CFM (molar $CaO/(FeO_T+MgO)$) diagram (Fig. 14E; Altherr et al., 2000), most of them plot in the field of partial melting products from metagreywackes. Similarly, they fall in the intervening areas of melting products from high-K mafic rocks, tonalites, and metasediments in the $3CaO$-$Al_2O_3/(FeO_T+MgO)$-$5K_2O/Na_2O$ diagram (Fig. 14F), reflecting a metagreywacke-like source (Patiño Douce, 1999). Fractionated normalized REE patterns, high total REE contents and negligible Eu anomalies of samples 13PQ10-1, 13PQ12-1, and 13PQ13-3 suggest a lower crust source below the stability field of plagioclase (>8kbar; Fig. 10E; Moyen and Martin, 2012). Sample 13PQ17-1 has the lowest TREE content and a concave-upward normalized REE pattern with positive Eu and negative Sr anomalies (Fig. 10E-F). This may be ascribed to the combined effects of residual plagioclase and hornblende, i.e., plagioclase triggers negative Sr and Eu anomalies, whereas hornblende contributes to low TREE contents (D_{TREE}(Hb)»1), which can further offset the negative Eu anomalies caused by plagioclase in the residue (Rollinson, 1993). Therefore, parental magmas of sample 13PQ17-1 could have been derived from a middle crust source within stability field of plagioclase (Fig. 10E-F). Neoarchean granitic rocks from different crustal levels have been reported in Northern Liaoning and Western Shandong (Wan et al., 2012; Wang et al., 2016).

6.3. Late Neoarchean crust-mantle geodynamics of Northern Hebei Province

Compared to the Nb/Ta ratios of chondrite and average continental crust (~12-17.6), most Pingquan samples have moderate to high Nb/Ta ratios of 15.50-32.58, similar to those of the Huai'an-Xuanhua granitoid gneisses (13.10-27.13, Fig. 15A; Weyer et al., 2002; Liu et al., 2012b). Except for the monzogranitic gneisses, the other basement rocks in the Pingquan Complex were differentiated from a lithospheric mantle metasomatized by recycled pelagic sediments (Fig. 8). Mantle melting and fractional crystallization cannot significantly fractionate Nb and Ta (Rollinson, 1993). The nearly chondrite-like Zr/Hf ratios argue against the involvement of carbonatite melts in the mantle source as a cause of the high Nb/Ta lithospheric mantle (Fig. 15B; Dupuy et al., 1992; Pfänder et al., 2012). Considering the above petrogenetic factors, we propose that partial melting of the subducted sediments (and/or oceanic basalts) within the stability field of rutile likely generated the high Nb/Ta melts that metasomatized the mantle wedge, serving as the sources of the Pingquan samples (Foley et al., 2002). The presence of rutile in the residue indicates a pressure of > 1.5 GPa (Xiong et al., 2005). A relatively lower slab surface temperature (~700-800 ℃) is favored to fulfill Nb/Ta ratios up to ~30 of the samples, implying a low thermal gradient of ~12-15℃/km (Hermann and Rubatto, 2009; Xiong et al., 2011; Fig. 15A). The lack of correlation between Zr/Hf and Lu/Hf suggests the involvement of partial melts from "zircon-free" pelagic sediments (Fig. 15B; Nebel et al., 2011).

For the entire Northern Hebei Province, though rare xenocrystic zircons (~2.7 Ga) were detected (Liu et al., 2007a; Wan et al., 2014, 2015), the lack of significant amounts of older crustal components (≥2.7 Ga) supports an oceanic setting for the evolution of the NHB (Supplementary Table 5 and Figs. 5, 12 and 13). Combined with the petrogenesis of representative lithologies and the low thermal gradient calculated above, the late Neoarchean (~2.55-2.50 Ga) crust-mantle geodynamic processes of the Northern Hebei Province can be summarized as follows. Intra-oceanic subduction was initiated offshore of the northwestern margin of the EB at ~2.55 Ga or earlier. With descending of the oceanic slabs, partial melting of the slab basalts occurred within the stability field of garnet and rutile, and the ascending melts were contaminated by the mantle wedge, which formed the ~2542-2499 Ma TTGs. Meanwhile, the sub-arc oceanic lithospheric mantle was metasomatized by fluids and melts derived from both the slab basalts and covered pelagic sediments. Partial melting of this moderately depleted lithospheric mantle generated both the ~2537-2508 Ma diorites and ~2506-2502 Ma (or older) basalts, and they experienced different degrees of fractional crystallization of clinopyroxene and/or hornblende. Notably, similar long-term subduction with a life span of ~50 Ma or more is characteristic of modern subduction zones (e.g., pan-African orogenic system and Hercynian Belt of W. Europe), implying that modern-style plate tectonics may have operated locally in the NCC during the late Neoarchean (Zhao, 2007; Moyen and Hunen, 2012 and references therein).

Development of the intra-oceanic arc resulted in gradual consumption of the ocean and final accretion of the arc terrane onto the continental margin of EB (Wang et al., 2015b, 2016). Subsequently, slab rollback/breakoff and asthenospheric mantle upwelling brought about high heat flux within the accreted arc-continent system. This triggered partial melting of the metasomatized lithospheric mantle and anatexis of the juvenile arc crust (metagreywackes) at ~2491 Ma, generating the quartz monzodioritic and the monzogranitic rocks. Although the monzogranitic gneisses show high Nb/Ta ratios, residual rutile was unnecessary as similarly high Nb/Ta ratios for possible protolith of early metabasaltic rocks and dioritic/TTG gneisses (Fig. 15A; Qian and Hermann, 2013).

6.4. Implications for late Neoarchean subduction-related crustal growth

Numerous zircon U-Pb and Lu-Hf isotopes have been obtained for early Precambrian basement rocks of NCC (e.g., Geng et al., 2012; Wang and Liu, 2012). While there is increasing accuracy of the temporal framework for the Archean geological events in the NCC, the timing of formation and evolution of continental crust remain debated due to reliance on isotopic model ages. In particular, the choice of different depleted mantle values may cause equivocal zircon Lu-Hf isotopic model ages (Vervoort and Kemp, 2016). In this study, the Pingquan basement rocks show zircon $\varepsilon Hf(t_2)$ values lower than the depleted mantle line (Fig. 8). Calculation of model ages according to the empirical $^{176}Lu/^{177}Hf$ value of the depleted mantle (0.0387; Blichert-Toft and Albarède, 1997) yield ages of ~2.7 Ga or older (Supplementary Table 3), which are widely taken as timing of crustal growth. However, as argued by Dhuime et al. (2011), new crust formed at intra-oceanic arcs show obviously lower $\varepsilon Hf(t)$ values than that of depleted mantle, resulting possibly from recycling of preexisting crustal materials to the mantle ever since ~3.0 Ga. Similarly, basement rocks of the NHB were derived from partial melting of either a moderately depleted mantle source (Fig. 8) with recycled pelagic sediments (metabasalts/dioritic/quartz monzodioritic gneisses) or juvenile oceanic slabs and metagreywackes (TTG and monzogranitic gneisses), recording apparent late Neoarchean (~2.6-2.5 Ga) crustal growth (Wang et al., 2015b). Phanerozoic subduction zones appear to be characterized by a balance between crustal growth and recycling, with zero net crustal growth (e.g., Scholl and Huene, 2009). However, Archean oceanic arcs could be thicker and more buoyant, which may have been accreted onto each other and resistant from being completely subducted (Condie and Kröner, 2013). Moreover, the Archean oceanic lithosphere is thick and buoyant (showing high Mg/Fe ratios), and its upper section, together with other buoyant subducted materials (e.g., pelagic sediments and arc lavas and plutons), may have "relaminated" back to the base of continental/arc crust instead of recycling to the deep mantle at the convergent margin setting (Hoffman and Ranalli, 1988; De wit, 1998; Hacker et al., 2011; Kelemen and Behn, 2016; Maunder et al., 2016).

The geodynamic regimes responsible for the Archean crustal growth remain enigmatic (Bédard, 2006, 2013, 2017; Cawood et al., 2006, 2013; Korenaga, 2013; Turner et al., 2014; Condie, 2016). Recent thermomechanical modeling reveals that plate tectonics could initiate at mantle temperatures ~175-250 □ higher than those of the present mantle, suggesting that the late Archean (< 3.2-3.0 Ga) may represent the transitional period from early stagnant-lid/plume tectonics to lateral plate tectonics (Herzberg, 2010; Gerya, 2014; Hawkesworth et al., 2017). These are further endorsed by the emergence of Meso- to Neoarchean paired metamorphic belts and especially eclogites, rapid development of potassic granitoids and decreasing production of komatiites, and increasing degree of crustal recycling (Condie and O'Neill, 2010; Mints et al., 2010; Dhuime et al., 2012, 2015; Laurent et al., 2014a). Similarly in the North China Craton, preliminary studies reveal that the geochemical features of

~3.8-2.5 Ga granitoids in Anshan changed during the Mesoarchean, possibly implying the transition from vertical processes (e.g., mantle overturn) to plate tectonics (Wan et al., 2015). The association of ~2.9 Ga intermediate-felsic volcanic rocks and TTG gneisses in the Jiaobei Terrane of the Eastern Block was considered to have been formed in an island arc setting (Jahn et al., 2008). However, whether subduction-accretion or mantle plume processes are the major tectonic regimes for the Neoarchean crustal growth and evolution of the Eastern Block is still hotly debated (Liu et al., 2002, 2004, 2011a; Geng et al., 2010; Wang et al., 2011, 2015b, 2016; Zhao et al., 2012; Wu et al., 2016a). As documented above, basement rocks of the Pingquan Complex were mainly formed by the partial melting of a moderately depleted lithospheric mantle metasomatized by subducted pelagic sediments, and record prolonged late Neoarchean crust-mantle geodynamic processes probably related to oceanic subduction and lateral arc-continent accretion. MORB-type metabasaltic rocks (i.e., fragments of oceanic crust) were not recognized in the metavolcanic rock assemblages of Northern Hebei (Figs. 3A and 10A-B). Some MORB-type metabasaltic rocks were identified in the Saheqiao area of Eastern Hebei (Guo et al., 2013). They yield a younger age (~2525 Ma) than the arc-related rocks (~2614-2518 Ma), and were interpreted to be generated in a back-arc environment. Nonetheless, apparent temporal and compositional variations of basement rocks are observed along the northern part of the Eastern Block (Liu et al., 2015; Fig. 1B), i.e., from northwest to southeast: (1) MORB-like metabasaltic rocks (~2.64-2.60 Ga) in the Fuxin area of the northernmost part of Western Liaoning; (2) in the southern part of Western Liaoning, Zunhua-Qinglong Block of Eastern Hebei, as well as Northern Hebei Province in this study, voluminous ~2.55-2.50 Ga dioritic to TTG gneisses and subordinate island arc tholeiitic to calc-alkaline metavolcanic rocks are dominated; and (3) ~2.52-2.48 Ga potassium-rich quartz monzodiorites, granodiorites, monzogranites, and K-feldspar granites are prevalent along the northern coast of Bohai Sea, i.e., Jinzhou-Qinhuangdao areas in Eastern Hebei and Western Liaoning. The above lateral variation of late Neoarchean basement rocks appears to be more compatible with subduction-related geodynamic regimes (Liu et al., 2015). This is further supported by the paired type of metamorphism established in the Eastern Hebei, recording contrasting geothermal gradients of ~40 ℃/km and ~20 ℃/km, respectively (Yang and Wei, 2017).

The Neoarchean intra-oceanic arc system of EB shows the following along-arc variations in character (Liu et al., 2004, 2012b, 2016; Wan et al., 2005; Wang, 2009; Wang et al., 2011, 2015b, 2016; Guo et al., 2013, 2015a; Peng et al., 2015; Wu et al., 2016a): (1) mafic to intermediate rocks in the NHB and Northern Liaoning have moderately depleted zircon $\varepsilon Hf(t)$ and/or whole-rock $\varepsilon Nd(t)$ values, distinct from those of Western Liaoning, Eastern Hebei, and Wutai Complex where island-arc tholeiitic to calc-alkaline basalts show isotopic compositions more close to those of the depleted mantle (Supplementary Table 6); and (2) basement rocks of the NHB and Northern Liaoning are mainly granitoid gneisses with intermediate to felsic compositions, whereas more meta-basaltic/andesitic rocks outcrop in Western Liaoning, Eastern Hebei, and Wutai Complex, associated with prolific gold and BIF-type iron deposits (Zhai and Santosh, 2013). Accordingly, a linkage between the nature of sub-arc lithospheric mantle and average compositions of arc crust can be established: arc segment coupled with more enriched lithospheric mantle tends to produce more felsic crust. Therefore, crustal recycling (especially sediment subduction) via plate tectonics may potentially lead to the formation of more felsic juvenile Archean crust (Dhuime et al., 2015; Tang et al., 2016).

In summary, the NHB records subduction-related crustal growth in the late Neoarchean. Intra-oceanic arc magmatism and arc-continent accretion could be an effective crust-mantle geodynamic regime responsible for Neoarchean crustal growth along northwestern margin of EB (Condie and Kröner, 2013; Santosh et al., 2013; Nutman et al., 2015; Wang et al., 2015b).

7. Conclusions

(1) The Pingquan Complex in the eastern part of Northern Hebei Province (NHB) consists of ~2537-2515 Ma dioritic gneisses, ~2506-2503 Ma amphibolites, and ~2491 Ma quartz monzodioritic to monzogranitic gneisses.

(2) Integrated with granitoid gneisses and metabasalts from Huai'an-Xuanhua and Dantazi complexes of whole NHB, it is suggested that metabasalts were derived from partial melting of a moderately depleted mantle source, with melts subjected to clinopyroxene and hornblende fractionation. Dioritic gneisses were produced by partial melting of a similar moderately depleted mantle source, and experienced fractionation of clinopyroxene and minor plagioclase. Quartz monzodioritic and monzogranitic gneisses were generated respectively by partial melting of a moderately depleted mantle source and juvenile metagreywackes.

(3) Neoarchean crust-mantle geodynamic processes of the NHB are summarized as follows. Intra-oceanic subduction initiated offshore of the continental margin of EB at ~2.55 Ga or earlier. At ~2542-2499 Ma, partial melting of slab basalts occurred, with the melts contaminated by mantle wedge materials forming TTG rocks. Meanwhile, sub-arc lithospheric mantle was enriched by fluids and melts derived from both slab basalts and pelagic sediments,

and partial melting of this moderately depleted mantle generated ~2537-2508 Ma dioritic and ~2506-2502 Ma basaltic rocks. The pelagic sediments should have been metamorphosed to rutile-bearing eclogites before melting. With consumption of the intervening ocean, the oceanic arc finally accreted onto continental margin of EB, and the resultant slab rollback/breakoff and asthenospheric mantle upwelling induced partial melting of the metasomatized lithospheric mantle and crustal anatexis, forming ~2491 Ma quartz monzodioritic and monzogranitic rocks.

(4) The NHB was evolved under a late Neoarchean subduction-related tectonic setting, and records significant Neoarchean crustal growth linked to lateral intra-oceanic subduction and arc-continent accretion.

Acknowledgments

We would like to express our thanks to Editor Guochun Zhao, Guest Editor Jian Zhang, Allen Nutman, and one anonymous reviewer, whose constructive suggestions and comments have led to great improvements in the quality of this manuscript. We also appreciate laboratory assistance offered by Dr. L. Su at the Geological Lab Center, China University of Geosciences, Beijing, and Dr. Z.C. Hu at the state Key Laboratory of Geological Processes and Mineral Resources, China University of Geosciences in Wuhan. This study is financially supported by the National Natural Science Foundation of China (Grant Nos. 41530207, 41502179, 41472165, 41602198) and Central University Basic Scientific Research Business Expenses (Grant No. 2652015038). PAC acknowledges support from Australian Research Council grant FL160100168.

References

Altherr, R., Holl, A., Hegner, E., 2000. High-potassium, calc-alkaline I-type plutonism in the European Variscides: Northern Vosges (France) and northern Schwarzwald (Germany). Lithos 50, 51-73.

Anderson, T., 2002. Correlation of common lead in U-Pb analyses that do not report ^{204}Pb. Chemical Geology 192, 59-79.

Bai, X., Liu, S.W., Guo, R.R., Zhang, L.F., Wang, W., 2014a. Zircon U-Pb-Hf isotopes and geochemistry of Neoarchean dioritic-trondhjemitic gneisses, Eastern Hebei, North China Craton: constraints on petrogenesis and tectonic implications. Precambrian Research 251, 1-20.

Bai, X., Liu, S.W., Zhang, L.F., Yan, M., Wang, W., Guo, R.R., Guo, B.R., 2014b. Geological event series of Early Precambrian complex in South Fushun area, Liaoning Province. Acta Petrologica Sinica 30, 2905-2924 (in Chinese with English abstract).

Bai, X., Liu, S.W., Guo, R.R., Wang, W., 2015. Zircon U-Pb-Hf isotopes and geochemistry of two contrasting Neoarchean charnockitic rock series in Eastern Hebei, North China Craton: Implications for petrogenesis and tectonic setting. Precambrian Research 267, 72-93.

Bai, X., Liu, S.W., Guo, R.R., Wang, W., 2016. A Neoarchean arc-back-arc system in Eastern Hebei, North China Craton: constraints from zircon U-Pb-Hf isotopes and geochemistry of dioritic-tonalitic-trondhjemitic-granodioritic (DTTG) gneisses and felsic paragneisses. Precambrian Research 273, 90-111.

Bédard, J.H., 2006. A catalytic delamination-driven model for coupled genesis of Archaean crust and sub-continental lithospheric mantle. Geochimica et Cosmochimica Acta 70, 1188-1214.

Bédard, J.H., 2013. How many arcs can dance on the head of a plume?: a ‘Comment’ on: A critical assessment of Neoarchean ‘plume only’ geodynamics: evidence from the Superior province, by Derek Wyman, Precambrian Research, 2012. Precambrian Research 229, 189-197.

Bédard, J.H., 2017. Stagnant lids and mantle overturns: Implications for Archaean tectonics, magmagenesis, crustal growth, mantle evolution, and the start of plate tectonics. Geoscience Frontiers, doi:10.1016/j.gsf.2017.01.005.

Blichert-Toft, J., Albarède, F., 1997. The Lu-Hf geochemistry of chondrites and the evolution of the mantle-crust system. Earth and Planetary Science Letters 148, 243-258.

Caro, G., Bourdon, B., 2010. Non-chondritic Sm/Nd ratio in the terrestrial planets: consequences for the geochemical evolution of the mantle-crust system. Geochimica et Cosmochimica Acta 74, 3333-3349.

Carpentier, M., Chauvel, C., Maury, R.C., Mattielli, N., 2009. The “zircon effect” as recorded by the chemical and Hf isotopic compositions of Lesser Antilles forearc sediments. Earth and Planetary Science Letters 287, 86-99.

Cawood, P.A., Kröner, A., Pisarevsky, S., 2006. Precambrian plate tectonics: Criteria and evidence. GSA today 16, 4-11.

Cawood, P.A., Hawkesworth, C.J., Dhuime, B., 2013. The continental record and the generation of continental crust. Geological Society of American Bulletin 125, 14-32.

Chauvel, C., Blichert-Toft, J., 2001. A hafnium isotope and trace element perspective on melting of the depleted mantle. Earth and Planetary Science Letters 190, 137-151.

Clemens, J.D., Stevens, G., 2012. What controls chemical variation in granitic magmas? Lithos 134-135, 317-329.

Condie, K.C., Belousova, E., Griffin, W.L., Sircombe, K.N., 2009. Granitoid events in space and time: Constraints from igneous and detrital zircon age spectra. Gondwana Research 15, 228-242.

Condie, K.C., O'Neill, C., 2010. The Archean-Proterozoic boundary: 500 My of tectonic transition in Earth History. American Journal of Science 310, 775-790.

Condie, K.C., Kröner, A., 2013. The building blocks of continental crust: evidence for a major change in the tectonic setting of continental growth at the end of the Archean. Gondwana Research 23, 394-402.

Condie, K.C., 2016. A planet in transition: The onset of plate tectonics on Earth between 3 and 2 Ga? Geoscience Frontiers, doi: 10.1016/j.gsf.2016.09.001.

Corfu, F., Hanchar, J.M., Hoskin, P.W.O., Kinny, P., 2003. Atlas of zircon textures. In: Hanchar, J.M., Hoskin, P.W.O. (Eds.), Mineralogical Society of America Reviews in Mineralogy and Geochemistry 53. Zircon, pp. 469-500.

Couzinié, S., Laurent, O., Moyen, J.F., Zeh, A., Bouihol, P., Villaros, A., 2016. Post-collisional magmatism: Crustal growth not identified by zircon Hf-O isotopes. Earth and Planetary Science Letters 456, 182-195.

De wit, M.J., 1998. On Archean granites, greenstones, cratons and tectonics: does the evidence demand a verdict? Precambrian Research 91, 181-226.

Deng, H., Kusky, T., Polat, A., Wang, C., Wang, L., Li, Y.X., Wang, J.P., 2016. A 2.5 Ga fore-arc subduction-accretion complex in the Dengfeng granite-greenstone belt, Southern North China Craton. Precambrian Research 275, 241-264.

Dhuime, B., Hawkesworth, C., Cawood, P., 2011. When continents formed. Science 331, 154-155.

Dhuime, B., Hawkesworth, C.J., Cawood, P.A., Storey, C.D., 2012. A Change in the geodynamics of continental growth 3 billion years ago. Science 335, 1334-1336.

Dhuime, B., Wuestefeld, A., Hawkesworth, C.J., 2015. Emergence of modern continental crust about 3 billion years ago. Nature Geoscience 8, 552–555.

Diwu, C.R., Sun, Y., Guo, A.L., Wang, H.L., Liu, X.M., 2011. Crustal growth in the North China Craton at ~2.5 Ga: evidence from in situ zircon U-Pb ages, Hf isotopes and whole-rock geochemistry of the Dengfeng complex. Gondwana Research 20, 149-170.

Dupuy, C., Liotard, J.M., Dostal, J., 1992. Zr/Hf fractionation in intraplate basaltic rocks: carbonate metasomatism in the mantle source. Geochimica et Cosmochimica Acta 6, 2417-2423.

Foley, S., Tiepolo, M., Vannucci, R., 2002. Growth of early continental crust controlled by melting of amphibolite in subduction zones. Nature 417, 837-840.

Ge, S.S., Zhai, M.G., Li, T.S., Peng, P., Santosh, M., Shan, H.X., 2015. Zircon U-Pb geochronology and geochemistry of low-grade metamorphosed volcanic rocks from the Dantazi Complex: Implications for the evolution of the North China Craton. Journal of Asian Earth Sciences 111, 948-965.

Geng, Y.S., Shen, Q.H., Ren, L.D., 2010. Late Neoarchean to early Paleoproterozoic magmatic events and tectonothermal systems in the North China Craton. Acta

Petrologica Sinica 26, 1945-1966 (in Chinese with English abstract).

Geng, Y.S., Du, L.L., Ren, L.D., 2012. Growth and reworking of the early Precambrian continental crust in the North China Craton: constraints from zircon Hf isotopes. Gondwana Research 21, 517-529.

Gerya, T., 2014. Precambrian geodynamics: Constraints and models. Gondwana Research 25, 442-463.

Griffin, W.L., Pearson, N.J., Belousova, E., Jackson, S.E., van Achterbergh, E., O'Reilly, S.Y., Shee, S.R., 2000. The Hf isotope composition of cratonic mantle: LAM-MC-ICPMS analysis of zircon megacrysts in kimberlites. Geochimica et Cosmochimica Acta 64, 133-147.

Griffin, W.L., Belousova, E.A., O'Neill, C., O'Reilly, S.Y., Malkovets, V., Pearson, N.J., Spetsius, S., Wilde, S.A., 2014. The world turns over: Hadean-Archean crust-mantle evolution. Lithos 189, 2-15.

Grove, T.L., Till, C.B., Krawczynski, M.J., 2012. The role of H_2O in subduction zone magmatism. Annual Review of Earth and Planetary Sciences 40, 413-439.

Guo, J.H., O'Brien, P.J., Zhai, M.G., 2002. High-pressure granulites in the Sanggan area, North China craton: metamorphic evolution, P-T paths and geotectonic significance. Journal of Metamorphic Geology 20, 741-756.

Guo, J.H., Sun, M., Chen, F.K., Zhai, M.G., 2005. Sm-Nd and SHRIMP U-Pb zircon geochronology of high-pressure granulites in the Sanggan area, North China Craton: timing of Paleoproterozoic continental collision. Journal of Asian Earth Sciences 24, 629-642.

Guo, J.H., Peng, P., Chen, Y., Jiao, S.J., Windley, B.F., 2012. UHT sapphirine granulite metamorphism at 1.93-1.92 Ga caused by gabbronorite intrusions: implications for tectonic evolution of the northern margin of the North China Craton. Precambrian Research 222-223, 124-142.

Guo, R.R., Liu, S.W., Santosh, M., Li, Q.G., Bai, X., Wang, W., 2013. Zircon U–Pb–Hf isotopes and geochemistry of Neoarchean dioritic-trondhjemitic gneisses, Eastern Hebei, North China Craton: constraints on petrogenesis and tectonic implications. Gondwana Research 24, 664-686.

Guo, R.R., Liu, S.W., Wyman, D., Bai, X., Wang, W., Li, Q.G., Yan, M., 2015a. Neoarchean subduction: a case study of arc volcanic rocks in Qinglong-Zhuzhangzi area of the Eastern Hebei Province, North China Craton. Precambrian Research 264, 36-62.

Guo, B.R., Liu, S.W., Zhang, J., Yan, M., 2015b. Zircon U-Pb-Hf isotopic systematics and Whole-rock geochemistry of Jinchengdong Neoarchean granite-greenstone belt in the Southern Jilin Province: implications for the early Precambrian crustal evolution of North China Craton. Gondwana Research 271, 254-277.

Guo, J.H., Zhai, M.G., Peng, P., Jiao, S.J., Zhao, L., Wang, H.Z., 2015c. Paleoproterozoic granulites in the North China Craton and their geological implications. In: M. G. Zhai (Ed.), Precambrian Geology of China (pp. 137-169). Berlin: Springer.

Hacker, B.R., Kelemen, P.B., Behn, M.D, 2011. Differentiation of the continental crust by relamination. Earth and Planetary Science Letters 307, 501-516.

Handley, H.K., Turner, S., Macpherson, C.G., Gertisser, R., Davidson, J.P., 2011. Hf-Nd isotope and trace element constraints on subduction inputs at island arcs: limitations of

Hf anomalies as sediment input indicators. Earth and Planetary Science Letters 304, 212-223.

Hawkesworth, C.J., Cawood, P.A., Dhuime, B., Kemp, T.I.S., 2017. Earth's continental lithosphere through time. Annual Reivews of Earth and Planetary Sciences, doi:10.1146/annurev-earth-063016-020525.

Heilimo, E., Jaana, H., Andersen, T., Huhma, H., 2013. Neoarchean crustal recycling and mantle metasomatism: Hf-Nd-Pb-O isotope evidence from sanukitoids of the Fennoscandian shield. Precambrian Research 228, 250-266.

Hermann, J., Rubatto, D., 2009. Accessory phase control on the trace element signature of sediment melts in subduction zones. Chemical Geology 265, 512-526.

Herzberg, C., Condie, K., Korenage, J., 2010. Thermal history of the Earth and its petrological expression. Earth and Planetary Science Letters 292, 79-88.

Hiess, J., Bennett, V.C., 2016. Chondritic Lu/Hf in the early crust-mantle system as recorded by zircon populations from the oldest Eoarchean rocks of Yilgarn Craton, West Australia and Enderby Land, Antarctica. Chemical Geology 427, 125-143.

Hoffman, P.F., Ranalli, G., 1988. Archean oecanic flake tectonics. Geophysical Research Letters 15, 1077-1080.

Hoffmann, J.E., Münker, C., Polat, A., König, S., Mezger, K., Rosing, M.T., 2010. Highly depleted Hadean mantle reservoirs in the sources of early Archean arc-like rocks, Isua supracrustal belt, southern West Greenland. Geochimica et Cosmochimica Acta 74, 7236-7260.

Hu, Z.C., Liu, Y.S., Gao, S., Liu, W.G., Zhang, W., Tong, X.R., Lin, L., Zong, K.Q., Li, M., Chen, H.H., Zhou, L., Yang, L., 2012. Improved in situ Hf isotope ratio analysis of zircon using newly designed X skimmer cone and jet sample cone in combination with the addition of nitrogen by laser ablation multiple collector ICP-MS. Journal of Analytical Atomic Spectrometry 27, 1391-1399.

Jahn, B.M., Liu, D.Y., Wan, Y.S., Song, B., Wu, J.S., 2008. New U-Pb and Hf isotopic data confirm Anshan as the oldest preserved segment of the North China Craton. American Journal of Science 308, 232-269.

Kamber, B.S., 2015. The evolving nature of terrestrial crust from the Hadean, through the Archean, into the Proterozoic. Precambrian Research 258, 48-82.

Kelemen, P.B., Hanghoj, K., Greene, A.R., 2004. One view of the geochemistry of subduction-related magmatic arcs, with emphasis on primitive andesite and lower crust. In: Rudnick, R.L. (Ed.), The Crust, Treatise on Geochemistry, vol. 3. Elsevier, Netherlands, pp. 593-659.

Kelemen, P.B., Behn, M.D., 2016. Formation of lower continental crust by relamination of buoyant arc lavas and plutons. Nature Geoscience 9, 197-205.

Khanna, T.C., Bizimis, M., Yogodzinski, G.M., Mallick, S., 2014. Hafnium-neodymium isotope systematics of the 2.7 Ga Gadwal greenstone terrane, Eastern Dharwar craton, India: implications for the evolution of the Archean depleted mantle. Geochimica et Cosmochimica Acta 127, 10-24.

Kemp, A.I.S., Wilde, S.A., Hawkesworth, C.J., Coath, C.D., 2010. Hadean crustal evolution revisited: new constraints for Pb-Hf isotope systematics of the Jack Hills zircons. Earth and Planetary Science Letters 296, 45-56.

Korenaga, J., 2013. Initiation and evolution of plate tectonics on Earth: Theories and observations. Annual Review of Earth and Planetary Sciences 41, 117-151.

Kusky, T.M., 2011. Geophysical and geological tests of tectonic models of the North China Craton. Gondwana Research 20, 26-35.

Laurent, O., Doucelance, R., Martin, H., Moyen, J.F., 2013. Differentiation of the late-Archaean sanukitoid series and some implications for crustal growth: Insights from geochemical modelling on the Bulai pluton, Central Limpopo Belt, South Africa. Precambrian Research 227, 186-203.

Laurent, O., Rapopo, M., Stevens, G., Moyen, J.F., Martin, H., Doucelance, R., Bosq, C., 2014a. Contrasting petrogenesis of Mg-K and Fe-K granitoids and implications for post-collisional magmatism: case study from the Late-Archean Matok pluton (Pietersburg block, South Africa). Lithos 196-197, 131-149.

Laurent, O., Martin, H., Moyen, J.F., Doucelance, R., 2014b. The diversity and evolution of late-Archean granitoids: evidence for the onset of “modern-style” plate tectonics between 3.0 and 2.5 Ga. Lithos 205, 208-235.

Li, S.Z., Zhao, G.C., 2007. SHRIMP U-Pb zircon geochronology of the Liaoji granitoids: constraints on the evolution of the Paleoproterozoic Jiao-Liao-Ji belt in the Eastern Block of the North China Craton. Precambrian Research 158, 1-16.

Liu, S.W., Pan, Y.M., Li, J.H., Zhang, J., Li, Q.G., 2002. Geological and isotopic geochemical constraints on the evolution of the Fuping Complex, North China Craton. Precambrian Research 117, 41-56.

Liu, S.W., Pan, Y.M., Xie, Q.L., Zhang, J., Li, Q.G., 2004. Archean geodynamics in the Central

Zone, North China craton: constraints from geochemistry of two contrasting series of granitoids in the Fuping and Wutaishan complexes. Precambrian Research 130, 229-249.

Liu, S.W., Tian, W., Lv, Y.J., Li, Q.G., Feng, Y.G., Park, K.H., Song, Y.S., 2006. Geochemistry, Nd isotopic characteristics of metamorphic complexes in Northern Hebei: implications for crustal accretion. Acta Geologica Sinica 80, 807-818.

Liu, S.W., Lü, Y.J., Feng, Y.G., Zhang, C., Tian, W., Yan, Q.R., Liu, X.M., 2007a. Geology and zircon U-Pb isotopic chronology of Dantazi Complex, Northern Hebei Province. Geological Journal of China Universities 13, 484-497 (in Chinese with English abstract).

Liu, S.W., Lü, Y.J., Feng, Y.G., Liu, X.M., Yan, Q.R., Zhang, C., Tian, W., 2007b. Zircon and monazite geochronology of the Hongqiyingzi complex, northern Hebei, China. Geological Bulletin of China 26, 1086-1100 (in Chinese with English abstract).

Liu, D.Y., Wilde, S.A., Wan, Y.S., Wu, J.S., Zhou, H.Y., Dong, C.Y., Yin, X.Y., 2008. New U-Pb and Hf isotopic data confirm Anshan as the oldest preserved segment of the North China Craton. American Journal of Science 308, 200-231.

Liu, F., Guo, J.H., Lu, X.P., Diwu, C.R., 2009. Crustal growth at ~2.5 Ga in the North China Craton: evidence from whole-rock Nd and zircon Hf isotopes in the Huai'an gneiss terrane. Chinese Science Bulletin 54, 4704-4713.

Liu, S.W., Wang, W., Bai, X., Zhang, F., 2010. Geological events of early Precambrian complex in North Chaoyang area, Liaoning Province. Acta Petrologica Sinica 26, 1993-2004 (in Chinese with English abstract).

Liu, S.W., Santosh, M., Wang, W., Bai, X., Yang, P.T., 2011a. Zircon U-Pb chronology of the

Jianping Complex: implications for the Precambrian crustal evolution history of the northern margin of North China Craton. Gondwana Research 20, 48-63.

Liu, S.W., Lv, Y.J., Wang, W., Yang, P.T., Bai, X., Feng, Y.G., 2011b. Petrogenesis of the Neoarchean granitoid gneisses in northern Hebei Province. Acta Petrologica Sinica 27, 909-921 (in Chinese with English abstract).

Liu, S.W., Zhang, J., Li, Q.G., Zhang, L.F., Wang, W., Yang, P.T., 2012a. Geochemistry and U-Pb zircon ages of metamorphic volcanic rocks of the Paleoproterozoic Lüliang Complex and constraints on the evolution of the Trans-North China Orogen, North China Craton. Precambrian Research 222-223, 173-190.

Liu, F., Guo, J.H., Peng, P., Qian, Q., 2012b. Zircon U-Pb ages and geochemistry of the Huai'an TTG gneisses terrane: petrogenesis and implications for ~2.5 Ga crustal growth in the North China Craton. Precambrian Research 212-213, 225-244.

Liu, J.H., Liu, F.L., Ding, Z.J., Liu, C.H., Yang, H., Liu, P.H., Wang, F., Meng, E., 2013. The growth, reworking and metamorphism of early Precambrian crust in the Jiabei terrane, the North China Craton: constraints from U-Th-Pb and Lu-Hf isotopic systematics, and REE concentrations of zircon from Archean granitoid gneisses. Precambrian Research 224, 287-303.

Liu, F.L., Liu, P.H., Wang, F., Liu, J.H., Meng, E., Cai, J., Shi, J.R., 2014. U-Pb dating of zircons from granitic leucosomes in migmatites of the Jiaobei Terrane, southwestern Jiao-Liao-Ji Belt, North China Craton: Constraints on the timing and nature of partial melting. Precambrian Research 245, 80-89.

Liu, S.W., Wang, W., Bai, X., Guo, R.R., Guo, B.R., Hu, F.Y., Fu, J.H., Wang, M.J., 2015.

Precambrian geodynamics (VII): Formation and evolution of early continental crust. Earth Science Frontiers 22, 97-108 (in Chinese with English abstract).

Liu, C.H., Zhao, G.C., Liu, F.L., Shi, J.R., 2016. Constraints of volcanic rocks of the Wutai Complex (Shanxi Province, Northern China) on a giant late Neoarchean intra-oceanic arc system in the Trans-North China Orogen. Journal of Asian Earth Sciences 123, 178-212.

Ludwig, K.R., 2003. Berkeley Geochronology Center Special Publication, vol. 4.

Martin, H., 1986. Effect of steeper Archean geothermal gradient on geochemistry of subduction-zone magmas. Geology 14, 753-756.

Martin, H., Smithies, R.H., Moyen, J.F., Champion, D., 2005. An overview of adakite, tonalite-trondhjemite-granodiorite (TTG), and sanukitoid: relationships and some implications for crust evolution. Lithos 79, 1-24.

Martin, H., Moyen, J.F., Rapp, R., 2010. The sanukitoid series: magmatism at the Archaean-Proterozoic transition. In: Sixth Hutton Symposium on the Origin of Granites and Related Rocks: Proceedings of a Symposium Held in Stellenbosch, South Africa, 2-6 July 2007. Cambridge University Press, p.15.

Maunder, B., van Hunen, J., Magni, V., Bouihol, P., 2016. Relamination of mafic subducting crust throughout Earth's history. Earth and Planetary Science Letters 449, 206-216.

Middlemost, E.A.K., 1994. Naming materials in magma/igneous rock system. Earth-Science Reviews 37, 215-224.

Mints, M.V., Belousova, E.A., Konilov, A.N., Natapov, L.M., Shchipansky, A.A., Griffin, W.L., O'Reilly, S.Y., Dokukina, K.A., Kaulina, T.V., 2010. Mesoarchean subduction processes:

2.87 Ga eclogites from the Kola Peninsula, Russia. Geology 38, 739-742.

Moyen, J.F., Martin, H., Jayananda, M., Auvray, B., 2003. Late Archaean granites: a typology based on the Dharwar Craton (India). Precambrian Research 127, 103-123.

Moyen, J.F., Martin, H., 2012. Forty years of TTG research. Lithos 148, 312-336.

Moyen, J.F., van Hunen, J., 2012. Short-term episodicity of Archean plate tectonics. Geology 40, 451-454.

Nebel, O., Vroon, P.Z., van Westrenen, W., Iizuka, T., Davies, G.R., 2011. The effect of sediment recycling in subduction zones on the Hf isotope character of new arc crust, Banda arc, Indonesia. Earth and Planetary Science Letters 303, 240-250.

Nutman, A.P., Wan, Y.S., Du, L.L., Friend, C.R.L., Dong, C.Y., Xie, H.Q., Wang, W., Sun, H.Y., Liu, D.Y., 2011. Multistage late Neoarchaean crustal evolution of the North China Craton, eastern Hebei. Precambrian Research 189, 43-65.

Nutman, A.P., Bennett, V.C., Friend, C.R.L., Yi, K., Lee, S.R., 2015. Mesoarchaean collision of Kapisilik terrane 3070 Ma juvenile arc rocks and >3600 Ma Isukasia terrane continental crust (Greenland). Precambrian Research 258, 146-160.

O'Connor, J.T., 1965. A classification for quartz-rich igneous rocks based on feldspar ratios. U.S. Geological Survey Professionnal Paper, 525, pp. 79-84.

O'Neil, J., Carlson, R.W., Francis, D., Stevenson, R.K., 2008. Neodymium-142 evidence for Hadean mafic crust. Science 321, 1828-1831.

O'Neil, J., Rizo, H., Boyet, M., Carlson, R.W, Rosing, M.T., 2016. Geochemistry and Nd isotopic characteristics of Earth's Hadean mantle and primitive crust. Earth and Planetary Science Letters 442, 194-205.

Patiño Douce, A.E., 1999. What do experiments tell us about the relative contributions of crust and mantle to the origin of granitic magmas? Geological Society, London, Special Publications 168, 55-75.

Payne, J.L., McInerney, D.J., Barovich, K.M., Kirkland, C.L., Pearson, N.J., Hand, M., 2016. Strengths and limitations of zircon Lu-Hf and O isotopes in modelling crustal growth. Lithos 248-251, 175-192.

Pearce, J.A., Peate, D.W., 1995. Tectonic implications of the composition of volcanic arc magmas. Annual Review of Earth and Planetary Sciences 24, 251-285.

Pearce, J.A., 2014. Geochemical fingerprinting of the Earth's oldest rocks. Geology 42, 175-176.

Peng, P., Zhai, M.G., Ernst, R.E., Guo, J.H., Liu, F., Hu, B., 2008. A 1.78 Ga large igneous province in the North China craton: the Xiong'er Volcanic Province and the North China dyke swarm. Lithos 101, 260-280.

Peng, P., Li, Y., Liu, F., Wang, F., 2012. Geological relation of late Archean lithologic units in Northwest Hebei, North China Craton: implications for building of early continental crust. Acta Petrologica Sinica 28, 3531-3544 (in Chinese with English abstract).

Peng, P., Wang, C., Wang, X.P., Yang, S.Y., 2015. Qingyuan high-grade granite-greenstone terrain in the Eastern North China Craton: Root of a Neoarchaean arc. Tectonophysics 662, 7-21.

Pfänder, J.A., Jung, S., Münker, C., Stracke, A., Mezger, K., 2012. A possible high Nb/Ta reservoir in the continental lithospheric mantle and consequences on the global Nb budget-evidence from continental basalts from Central Germany. Geochimica et

Cosmochimica Acta 77, 232-251.

Polat, A., Hofmann, A.W., 2003. Alteration and geochemical patterns in the 3.7-3.8 Ga Isua greenstone belt, West Greenland. Precambrian Res. 126, 197-218.

Qian, Q., Hermann, J., 2013. Partial melting of lower crust at 10-15 kbar: constraints on adakite and TTG formation. Contributions to Mineralogy and Petrology 165, 1195-1224.

Qu, J.F., Li, J.Y., Liu, J.F., 2012. Geochonological study on the Fenghuangzui Complex of Dantazi Goup at northern Hebei Province. Acta Petrologica Sinica 28, 2879-2889.

Rapp, R.P., Watson, E.B., 1995. Dehydration melting of metabasalt at 8-32 kbar: implications for continental growth and crust-mantle recycling. Journal of Petrology 36, 891-931.

Rollinson, H.R., 1993. Using Geochemical Data: Evaluation, Presentation, Interpretation. Pearson Education Limited, London, pp. 108-111.

Rollinson, H., 2010. Coupled evolution of Archean continental crust and subcontinental lithospheric mantle. Geology 38, 1083-1086.

Rollinson, H., 2015. Slab and sediment melting during subduction initiation: granitoid dykes from the mantle section of the Oman ophiolite. Contributions to Mineralogy and Petrology 170, 32.

Ross, P.S., Bédard, J.H., 2009. Magmatic affinity of modern and ancient subalkaline volcanic rocks determined from trace-element discriminant diagrams. Canadian Journal of Earth Sciences 46, 823-839.

Rubatto, D., 2002. Zircon trace element geochemistry: partitioning with garnet and the link between U–Pb ages and metamorphism. Chem. Geol. 184, 123-138.

Santosh, M., Tsunogae, T., Li, J.H., Liu, S.J., 2007. Discovery of sapphirine-bearing Mg-Al granulites in the North China Craton: implications for Paleoproterozoic ultrahigh temperature metamorphism. Gondwana Research 11, 263-285.

Santosh, M., 2010. Assembling North China Craton within the Columbia supercontinent: the role of double-sided subduction. Precambrian Research 178, 149-167.

Santosh, M., Shaji, E., Tsunogae, T., Mohan, M.R., Satyanarayanan, M., Horie, K., 2013. Suprasubduction zone ophiolite from Agali hill: Petrology, zircon SHRIMP U-Pb geochronology, geochemistry and implications for Neoarchean plate tectonics in southern India. Precambrian Research 231, 301-324.

Scholl, D.W., Huene, R.V., 2009. Implications of estimated magmatic additions and recycling losses at the subduction zones of accretionary (non-collisional) and collisional (suturing) orogens. Geological Society, London, Special Publications 318, 105-125.

Segal, I., Halicz, L., Platzner, I.T., 2003. Accurate isotope ratio measurements of ytterbium by multiple collection inductively coupled plasma mass spectrometry applying erbium and hafnium in an improved double external normalization procedure. Journal of Analytical Atomic Spectrometry 18, 1217-1223.

Söderlund, U., Patchett, P.J., Vervoort, J.D., Isachsen, C.E., 2004. The ^{176}Lu decay constant determined by Lu-Hf and U-Pb isotope systematics of Precambrian mafic intrusions. Earth and Planetary Science Letters 219, 311-324.

Sun, S.S., McDonough, W.F., 1989. Chemical and isotopic systematics of oceanic basalts: implication for mantle composition and processes. In: Saunders, A.D., Norry, M.J. (Eds.), Magmatism in Ocean Basins. Geological Society, London, Special Publication 42, pp. 313-345.

Tan, Y.J., Wang, G.C., Li, S.X., 1991. Archean geology and gold deposit prospecting direction in the Pingquan-Chengde area, Northern Hebei Province. China University of Geosciences Press, Wuhan (in Chinese), pp. 1-80.

Tang, M., Chen, K., Rudnick, R.L., 2016. Archean upper crust transition from mafic to felsic marks the onset of plate tectonics. Science 351, 372-375.

Tatsumi, Y., 2006. High-Mg andesites in the Setouchi volcanic belt, southwestern Japan: analogy to Archean magmatism and continental crust formation? Annual Review of Earth and Planetary Sciences 34, 467-499.

Treuil, M., Joron, J.M., 1975. Utilization des elements hydromagmayophiles pour la simplification de la modelisation quantitative des processes magmatiques. Exeples de l'Afar et de da dorsale medioatlantique. Rend. SMP 31, 125-174.

Tuner, S., Rushmer, T., Reagan, M., Moyen, J.F., 2014. Heading down early on? Start of subduction on Earth. Geology 42, 139-142.

van Achterbergh, E., Ryan, C., Jackson, S., Griffin, W.L., 2001. In: Sylvester, P. (Ed.), Appendix 3 Data Reduction Software for LA-ICP-MS in “Laser-Ablation-ICPMS in the Earth Sciences”: Mineralogical Association of Canada Short Course, pp. 239-243, vol. 29.

Vervoort, J.D., Kemp. A.IS., 2016. Clarifying the zircon Hf isotope record of crust-mantle evolution. Chemical Geology 425, 65-75.

Wan, Y.S., Song, B., Geng, Y.S., Liu, D.Y., 2005. Geochemical characteristics of Archean basement in the Fushun-Qingyuan area, Northern Liaoning Province and its geological significance. Geological Review 51, 128-137 (in Chinese with English abstract).

Wan, Y.S., Liu, D.Y., Wang, S.J., Dong, C.Y., Yang, E.X., Wang, W., Zhou, H.Y., Ning, Z.G., Du, L.L., Yin, X.Y., Xie, H.Q., Ma, M.Z., 2010. Juvenile magmatism and crustal recycling at the end of the Neoarchean in Western Shandong Province, North China Craton: evidence from SHRIMP zircon dating. American Journal of Science 310, 1503-1552.

Wan, Y.S., Dong, C.Y., Liu, D.Y., Kröner, A., Yang, C.H., Wang, W., Du, L.L., Xie, H.Q., Ma, M.Z., 2012. Zircon ages and geochemistry of late Neoarchean syenogranites in the North China Craton: A review. Precambrian Research 222-223, 265-289.

Wan, Y.S., Zhang, Y.H., Williams, I.S., Liu, D.Y., Dong, C.Y., Fan, R.L., Shi, Y.R., Ma, M.Z., 2013. Extreme zircon O isotopic compositions from 3.8 to 2.5 Ga magmatic rocks from the Anshan area, North China Craton. Chemical Geology 352, 108-124.

Wan, Y.S., Xie, S.W., Yang, C.H., Kröner, A., Ma, M.Z., Dong, C.Y., Du, L.L., Xie, H.Q., Liu, D.Y., 2014. Early Neoarchean (~2.7 Ga) tectono-thermal events in the North China Craton: a synthesis. Precambrian Research 247, 45-63.

Wan, Y.S., Liu, D.Y., Dong, C.Y., Xie, H.Q., Kröner, A., Ma, M.Z., Liu, S.J., Xie, S.W., Ren, P., 2015. Formation and evolution of Archean continental crust of the North China Craton. In: M. G. Zhai (Ed.), Precambrian Geology of China (pp. 59-136). Berlin: Springer.

Wang, Z.H., 2009. Tectonic evolution of the Hengshan-Wutai-Fuping complexes and its implication for the Trans-North China Orogen. Precambrian Research 170, 73-87.

Wang, W., Liu, S.W., Bai, X., Yang, P.T., Li, Q.G., Zhang, L.F., 2011. Geochemistry and zircon U-Pb-Hf isotopic systematics of the Neoarchean Yixian-Fuxin greenstone belt, northern margin of the North China Craton: implications for petrogenesis and tectonic setting. Gondwana Research 20, 64-81.

Wang, A.D., Liu, Y.C., 2012. Neoarchean (2.5-2.8 Ga) crustal growth of the North China Craton revealed by zircon Hf isotope: a synthesis. Geoscience Frontiers 3, 147-173.

Wang, W., Liu, S.W., Wilde, S.A., Li, Q.G., Zhang, J., Bai, X., Yang, P.T., Guo, R.R., 2012a. Petrogenesis and geochronology of Precambrian granitoid gneisses in Western Liaoning Province: constraints on Neoarchean to early Paleoproterozoic crustal evolution of North China Craton. Precambrian Research 222-223, 290-311.

Wang, W., Liu, S.W., Feng, Y.G., Li, Q.G., Wu, F.H., Wang, Z.Q., Wang, R.T., Yang, P.T., 2012b. Chronology, petrogenesis and tectonic setting of the Neoproterozoic Tongchang dioritic pluton at the northwestern margin of the Yangtze Block: constraints from geochemistry and zircon U-Pb-Hf isotopic systematics. Gondwana Research 22, 699-716.

Wang, W., Liu, S.W., Santosh, M., Bai, X., Li, Q.G., Yang, P.T., Guo, R.R., 2013. Zircon U-Pb-Hf isotopes and whole-rock geochemistry of granitoid gneisses in the Jianping gneissic terrane, Western Liaoning Province: constraints on the Neoarchean crustal evolution of the North China Craton. Precambrian Research 224, 184-221.

Wang, Y.F., Li, X.H., Jin, W., Zhang, J.H., 2015a. Eoarchean ultra-depleted mantle domains inferred from ca. 3.8 Ga Anshan trondhjemitic gneisses, North China Craton. Precambrian Research 263, 88-107.

Wang, W., Liu, S.W., Santosh, M., Wang, G.H., Bai, X., Guo, R.R., 2015b. Neoarchean intra-oceanic arc system in the Western Liaoning Province: implications for the Early Precambrian crust-mantle geodynamic evolution of the Eastern Block of the North China Craton. Earth-Science Reviews 150, 329-364.

Wang, W., Liu, S.W., Santosh, M., Deng, Z.B., Guo, B.R., Zhao, Y., Zhang, S.H., Yang, P.T., Bai, X., Guo, R.R., 2015c. Late Paleoproterozoic geodynamics of the North China Craton: Geochemical and zircon U-Pb-Hf records from a volcanic suite in the Yanliao rift. Gondwana Research 27, 300-325.

Wang, W., Liu, S.W., Cawood, P.A., Bai, X., Guo, R.R., Guo, B.R., Wang, K., 2016. Late Neoarchean subduction-related crustal growth in the Northern Liaoning region of the North China Craton: Evidence from ~2.55 to 2.50 Ga granitoid gneisses. Precambrian Research 281, 200-223.

Weyer, S., Münker, C., Rehkämper, M., Mezger, K., 2002. Determination of ultra low Nb, Ta, Zr, and Hf concentrations and precise Nb/Ta and Zr/Hf ratios by isotope dilution analyses with multiple collector ICP-MS. Chemical Geology 187, 295-313.

Whitehouse, M.J., Kamber, B.S., 2003. A rare earth element study of complex zircons from early Archean Amitsoq genisses, Godthabsfjord, south-west Greenland. Precambrian Research 126, 363-377.

Winchester, J.A., Floyd, P.A., 1976. Geochemical magma type discrimination: application to altered and metamorphosed basic igneous rocks. Earth and Planetary Science Letters 28, 459-469.

Woodhead, J.D., Hergt, J.M., Davidson, J.P., Eggins, S.M., 2001. Hafnium isotope evidence for ‘conservative’ element mobility during subduction processes. Earth and Planetary Science Letters 192, 331-346.

Wu, F.Y., Zhao, G.C., Wilde, S.A., Sun, D.Y., 2005. Nd isotopic constraints on crustal formation in the North China Craton. Journal of Asian Earth Sciences 24, 523-545.

Wu, F.Y., Yang, Y.H., Xie, L.W., Yang, J.H., Xu, P., 2006. Hf isotopic compositions of the

ACCEPTED MANUSCRIPT

standard zircons and baddeleyites used in U-Pb geochronology. Chemical Geology 234, 105-126.

Wu, M.L., Lin, S.F., Wan, Y.S., Gao, J.F., 2016a. Crustal evolution of the Eastern Block in the North China Craton: constraints from zircon U-Pb geochronology and Lu-Hf isotopes of the North Liaoning Complex. Precambrian Research 275, 35-47.

Wu, J.L., Zhang, H.F., Zhai, M.G., Guo, J.H., Liu, L., Yang, W.Q., Wang, H.Z., Zhao, L., Jia, X.L., Wang, W., 2016b. Discovery of pelitic high-pressure granulite from Manjinggou of the Huai'an Complex, North China Craton: Metamorphic P-T evolution and geological implications.

Xiong, X.L., Adam, J., Green, T.H., 2005. Rutile stability and rutile/melt HFSE partitioning during partial melting of hydrous basalt: Implications for TTG genesis. Chemical Geology 218, 339-359.

Xiong, X.L., Keppler, H., Audétat, A., Ni, H.W., Sun, W.D., Li, Y., 2011. Partitioning of Nb and Ta between rutile and felsic melt and the fractionation of Nb/Ta during partial melting of hydrous metabasalt. Geochimica et Cosmochimica Acta 75, 1673-1692.

Xu, B., Charvet, J., Chen, Y., Zhao, P., Shi, G.Z., 2013. Middle Paleozoic convergent orogenic belts in western Inner Mongolia (China): framework, kinematics, geochronology and implications for tectonic evolution of the Central Asian Orogenic Belt. Gondwana Research 23, 1342-1364.

Yang, Q.Y., Santosh, M., 2015. Paleoproterozoic arc magmatism in the North China Craton: No Siderian global plate tectonic shutdown. Gondwana Research 28, 82-105.

Yang, Q.Y., Santosh, M., Collins, A.S., Teng, X.M., 2016. Microblock amalgamation in the

North China Craton: Evidence from Neoarchaean magmatic suite in the western margin of the Jiaoliao Block. Gondwana Research 31, 96-123.

Yang, C., Wei, C.J., 2017. Ultrahigh temperature (UHT) mafic granulites in the East Hebei, North China Craton: Constraints from a comparison between temperatures derived from REE-based thermometers and major element-based thermometers. Gondwana Research 46, 156-169.

Yuan, H.L., Gao, S., Liu, X.M., Li, H.M., Günther, D., Wu, F.Y., 2004. Accurate U-Pb age and trace element determinations of zircon by laser ablation inductively coupled plasma-mass spectrometry. Geostandards and Geoanalytical Research 28, 353-370.

Zeh, A., Gerdes, A., Klemd, R., Barton, J.M.J., 2007. Archaean to Proterozoic Crustal Evolution in the Central Zone of the Limpopo Belt (South Africa-Botswana): constraints from Combined U-Pb and Lu-Hf Isotope Analyses of Zircon. Journal of Petrology 48, 1605-1639.

Zeh, A., Stern, R.A., Gerdes, A., 2014. The oldest zircons of Africa-Their U-Pb-Hf-O isotope and trace element systematics, and implications for Hadean to Archean crust-mantle evolution. Precambrian Research 241, 203-230.

Zhang, H.F., Zhai, M.G., Santosh, M., Diwu, C.R., Li, S.R., 2011. Geochronology and petrogenesis of Neoarchean potassic meta-granites from Huai'an Complex: Implications for the evolution of the North China Craton. Gondwana Research 20, 82-105.

Zhang, H.F., Zhai, M.G., Santosh, M., Li, S.R., 2012. Low-Al and high-Al trondhjemites in the Huai'an Complex, North China Craton: Geochemistry, zircon U-Pb and Hf isotopes, and implications for Neoarchean crustal growth and remelting. Journal of Asian Earth

Sciences 49, 203-213.

Zhang, D.D., Guo, J.H., Tian, Z.H., Liu, F., 2016. Discovery of pelitic high-pressure granulite from Manjinggou of the Huai'an Complex, North China Craton: Metamorphic P-T evolution and geological implications. Precambrian Research 280, 76-94.

Zhai, M.G., Santosh, M., 2011. The Early Precambrian odyssey of the North China Craton: a synoptic overview. Gondwana Research 20, 6-25.

Zhai, M.G., Santosh, M., 2013. Metallogeny of the North China Craton: Link with secular changes in the evolving Earth. Gondwana Research 24, 275-297.

Zhao, G.C., Wilde, S.A., Cawood, P.A., Lu, L.Z., 1998. Thermal evolution of Archean basement rocks from the eastern part of the North China carton and its bearing on tectonic setting. International Geology Reviews 40, 706-721.

Zhao, G.C., Sun, M., Wilde, S.A., Li, S.Z., 2005. Late Archean to proterozoic evolution of the North China Craton: Key issues revisited. Precambrian Research 136, 177-202.

Zhao, G.C., 2007. When did plate tectonics begin on the North China Craton? Insights from metamorphism. Earth Science Frontiers 14, 19-32 (in Chinese with English abstract).

Zhao, G.C., Wilde, S.A., Sun, M., Guo, J.H., Kröner, A., Li, S.Z., Li, X.P., Zhang, J., 2008. SHRIMP U-Pb zircon geochronology of the Huai'an Complex: constraints on Late Archean to Paleoproterozoic magmatic and metamorphic events in the Trans-North China Orogen. American Journal of Science 308, 270-303.

Zhao, G.C., Wilde, S.A., Guo, J.H., Cawood, P.A., Sun, M., Li, X.P., 2010. Single zircon grains record two Paleoproterozoic collisional events in the North China Craton. Precambrian Research 177, 266-276.

Zhao, G.C., Cawood, P.A., Li, S.Z., Wilde, S.A., Sun, M., Zhang, J., He, Y.H., Yin, C.Q., 2012. Amalgamation of the North China Craton: key issues and discussions. Precambrian Research 222-223, 55-76.

Figure Captions:

Fig. 1. (A) Geological sketch map of the North China Craton illustrating major early Precambrian basement terranes and late Paleoproterozoic tectonic framework (Zhao et al., 2005, 2012; Santosh, 2010). The Northern Hebei Province is marked by the rectangle. (B) Archean crust-mantle geodynamic model for the Eastern Block (EB) proposed by Wang et al. (2015b). The ~2.6-2.5 Ga intra-oceanic arc system established along the northwestern margin of EB records a major late Neoarchean episode of crustal growth linked to arc-continent accretion. Both Pingquan Complex (Fig. 2) and Northern Hebei Province (NHB) are marked by the rectangles. The distribution scopes of early Neoarchean and pre-Neoarchean basement terranes within EB are delineated. Abbreviations: CD-Chengde; DF-Dengfeng; EH-Eastern Hebei; FP-Fuping; HA-Huai'an; HS-Hengshan; JD-Jiaodong; LL-Lvliang; NL-Northern Liaoning; SJ-Southern Jilin; SL-Southern Liaoning; TH-Taihua; WL-Western Liaoning; WT-Wutai; WS-Western Shandong; XH-Xuanhua; ZH-Zanhuang; ZT-Zhongtiao.

Fig. 2. Detailed geological map of the Pingquan Complex showing regional geological setting and sampling locations (dated samples are marked by the red squares).

Fig. 3. Field photographs of Archean crystalline basement in the Pingquan Complex, showing

(A) intercalated supracrustal rocks of amphibolites and banded iron formations (BIFs); (B-C) dioritic gneisses that were locally intruded by monzogranitic gneisses; (D) dioritic gneisses that were emplaced by quartz monzodioritic gneisses, with local preservation of dioritic gneisses within quartz monzodioritic gneisses (E); and (F) pink monzogranitic gneisses. The scale bars of geologist, hammer, pencil, and card are ~175, ~30, ~15, and ~10 cm, respectively.

Fig. 4. Photomicrographs for representative late Neoarchean rock samples in the Pingquan Complex: amphibolite samples with (A-B) gneissic (sample 13PQ07-1) and (C) mylonitic structures (sample 13PQ16-3; leucocratic and melanocratic domains are hornblende and plagioclase, respectively); (D-E) dioritic gneiss sample 13PQ14-3 showing fine granulation and dynamic recrystallization, and pyroxene crystals constitute the porphyroblasts; (F) quartz dioritic gneiss sample 13PQ18-1; (G) quartz monzodioritic gneiss sample 13PQ11-8; and (H) monzogranitic gneiss sample 13PQ13-3. (+) – viewed under crossed polarized light; (–) – viewed under plane polarized light. Abbreviations: Cpx - clinopyroxene; Opx - orthopyroxene; Hb - hornblende; Bt - biotite; Pl - plagioclase; Kfs - potassic feldspar; Qz - quartz.

Fig. 5. Cathodoluminescence images (A and C) and concordia diagrams for LA-ICPMS zircon U-Pb isotopic age data (B and D) showing internal structures of zircon grains, analyzed domains, apparent $^{207}Pb/^{206}Pb$ ages and calculated ages of each zircon group for representative amphibolite samples 13PQ07-3 and 13PQ13-4.

Fig. 6. Cathodoluminescence images (A and C) and concordia diagrams for LA-ICPMS zircon

U-Pb isotopic age data (B and D) showing internal structures of zircon grains, analyzed domains, apparent $^{207}Pb/^{206}Pb$ ages and calculated ages of each zircon group for representative dioritic gneiss samples 13PQ14-3 and 13PQ16-4.

Fig. 7. Cathodoluminescence images (A) and concordia diagram for LA-ICPMS zircon U-Pb isotopic age data (B) showing internal structures of zircon grains, analyzed domains, apparent $^{207}Pb/^{206}Pb$ ages and calculated ages of each zircon group for representative quartz monzodioritic gneiss sample 13PQ11-8.

Fig. 8. Diagrams of initial $^{176}Hf/^{177}Hf(t_1)$ vs. apparent $^{207}Pb/^{206}Pb$ ages (t_1) (A, C, E, and G) and $\varepsilon Hf(t_2)$ values vs. crystallization ages (t_2) (B, D, F, and H) for samples 13PQ13-4, 13PQ14-3, 13PQ16-4, and 13PQ11-8. Comparable initial $^{176}Hf/^{177}Hf(t_1)$ values of most analyzed zircon domains for each sample (shaded areas) imply that they were originally crystallized from the same magmatic system, but subjected to different degrees of Pb loss (Zeh et al., 2007). $^{176}Lu/^{177}Hf$ ratios of depleted mantle and chondrite are 0.0384 and 0.0332, respectively (Blichert-Toft and Albarède, 1997; Griffin et al., 2000), whereas the “New Crust” evolution line indicates lower $\varepsilon Hf(t)$ values of juvenile crust generated in island arc settings, emphasizing the role of recycled sediments (Dhuime et al., 2011).

Fig. 9. Petrochemical classification and major geochemical features of representative samples of the Pingquan Complex. Late Neoarchean metabasaltic rocks and dioritic/TTG gneisses from the Dantazi and Huai’an-Xuanhua complexes of Northern Hebei Province are plotted for

comparison (Liu et al., 2011b, 2012b; Ge et al., 2015). (A) Zr/TiO_2*0.0001 vs. Nb/Y diagram (Winchester and Floyd, 1976) and (B) La vs. Yb discrimination diagram (Ross and Bédard, 2009) for metabasaltic rocks. Total alkalis vs. silica (TAS; Middlemost, 1994) (C); An-Ab-Or (O'Connor, 1965) (D); and MgO vs. SiO_2 (E) diagrams (PMB: experimentally-derived partial melts from metabasalts; LSA-low silica adakite; HSA-high silica adakite; Martin et al., 2005) for granitoid gneisses. Symbols: solid diamonds - amphibolites of Pingquan Complex; open diamonds - metabasaltic rocks of Dantazi Complex; solid squares - dioritic gneisses of Pingquan Complex; large/small open squares - dioritic/TTG gneisses of Huai'an-Xuanhua and Dantazi complexes; Solid triangles - quartz monzodioritic gneisses, and solid circles - monzogranitic gneisses of Pingquan Complex.

Fig. 10. Chondrite-normalized REE and primitive mantle-normalized multi-element patterns for (A-B) metabasaltic rocks; (C-D) dioritic and TTG gneisses; and (E-F) quartz monzodioritic and monzogranitic gneisses of Northern Hebei Province. Symbols are the same as Fig. 9, and chondrite and primitive mantle values after Sun and McDonough (1989).

Fig. 11. Summary of early Precambrian tectonothermal events in the Northern Hebei Province (detailed age data in Supplementary Table 5). (A) Histogram of major magmatic events, showing magmatic precursors of most supracrustal metavolcanic rocks and plutonic granitoid gneisses formed earlier than 2491 Ma. The inset illustrates detailed temporal framework of late Neoarchean to early Paleoproterozoic magmatic events. Magmatic precursors of sporadic granitic rocks were emplaced at ~2454-2410 and ~2003-1977 Ma, followed by the formation of

minor ~1859 Ma gabbroic rocks (two-pyroxene granulites); (B) histogram of major metamorphic events, showing early Paleoproterozoic age peaks at ~2480, ~2450, and ~2400 Ma and late Paleoproterozoic age peak at ~1850 Ma, with minor metamorphic zircon grains at ~2176-2065 Ma. Notably, eruption of ~2506-2502 Ma basaltic rocks (with subordinate andesitic to rhyolitic rocks) was earlier than the first episode of metamorphism (≤2488 Ma).

Fig. 12. Petrogenetic diagrams for metabasaltic rocks of Northern Hebei Province. (A) La/Sm vs. La diagram (Treuil and Joron, 1975), illustrating both partial melting and fractional crystallization trends; (B) CaO/Al_2O_3 vs. SiO_2 diagram, showing effects of clinopyroxene (Cpx) fractionation; (C) Fe_2O_3T vs. TiO_2 diagram (the inset is Fe_2O_3T vs. V diagram), precluding the involvement of magnetite fractionation; (D) $(Nb/La)_{PM}$ vs. $(La/Sm)_N$ diagram (Sun and McDonough, 1989); (E) Zr/Yb vs. Nb/Yb diagram (Pearce and Peate, 1995), showing the nature of mantle sources compared with those of N-MORBs and E-MORBs; and (F) Sm/Hf vs. initial $^{176}Hf/^{177}Hf$ diagram, depicting different trends for addition of partial melts from pelagic sediments and detrital-rich turbidites in the depleted mantle sources (Handley et al., 2011). Initial $^{176}Hf/^{177}Hf$ values for depleted mantle (0.281324-0.281459) are compiled from modern Atalantic, Pacific, and Indian N-MORBs of Chauvel and Blichert-Toft (2001) (C&B, 2001), which are calculated back to 2.5 Ga using a $^{176}Lu/^{177}Hf$ ratio of 0.0387 (Griffin et al., 2000). Sm/Hf ratios of 1.28-1.31 for depleted mantle are used here, considering average Sm/Hf ratio of 1.28 for modern N-MORBs (C&B, 2001) and 1.31 for N-MORB of Sun and McDounough (1989) (S&M, 1989). Clinopyroxene and/or hornblende fractionation from basaltic to andesitic magmas can decrease the Sm/Hf ratios (Handley et al., 2011). Samples GB30 and GB33 with

higher Fe_2O_3T contents and magnetite accumulation display lower La/Sm but higher $(Nb/La)_{PM}$ ratios, suggesting a distinct mantle source (see main text for explanation).

Fig. 13. Petrogenetic diagrams for dioritic and TTG gneisses of Northern Hebei Province. (A) $(La/Yb)_N$ vs. $(La)_N$ diagram, discriminating adakitic rocks from Phanerozoic arc basalitic-andesitic-dacitic-rhyolitic rocks (Martin, 1986); (B) La/Sm vs. La diagram (Treuil and Joron, 1975), with dioritic and TTG gneisses respectively controlled by partial melting and fractional crystallization. High La/Sm ratios and low La contents of some samples may be ascribed to plagioclase accumulation (Rollinson, 1993); (C) Gd/Yb vs. MgO diagram (Wang et al., 2015b). Similar Gd/Yb ratios precludes a genetic link between dioritic and TTG gneisses by hornblende fractionation; (D) CaO/Al_2O_3 vs. SiO_2 diagram, emphasizing clinopyroxene (Cpx) fractionation for dioritic magmas; (E) $(Nb/La)_{PM}$ vs. $(La/Sm)_N$ diagram (Sun and McDonough, 1989); and (F) Sm/Hf vs. initial $^{176}Hf/^{177}Hf$ diagram, indicating involvement of partial melts from subducted pelagic sediments in the mantle source of dioritic gneisses. Low Sm/Hf ratio of sample 13PQ16-4 is better explained by Cpx fractionation (Handley et al., 2011).

Fig. 14. Petrogenetic diagrams for quartz monzodioritic and monzogranitic gneisses of Pingquan Complex. (A) K_2O-Na_2O-CaO diagram, showing a sodium-rich trend (1) for TTG gneisses) and a potassium-rich trend (2) for sanukitoids, closepet-type granites, biotite granites, and two mica-granites (Moyen et al., 2003); (B) A/CNK vs. maficity (atomic (Fe + Mg)/100g samples) diagram (Clemens and Stevens, 2012); entrainment of peritectic garnet (Gt) and clinopyroxene (Cpx) in granitic magmas are marked by different trends; (C) Sm/Hf vs.

initial $^{176}Hf/^{177}Hf$ diagram (Handley et al., 2011); large scatter of Sm/Hf ratios (0.53-2.27) of all quartz monzodioritic gneisses may be ascribed to Cpx crystallization (Wang et al., 2016); (D) Gd/Yb vs. MgO diagram, precluding effects of hornblende fractionation (Wang et al., 2015b); (E) molar Al_2O_3/(MgO + FeO_T) (AFM) vs. molar CaO/(MgO + FeO_T) (CFM) diagram (Altherr et al., 2000); and (F) Al_2O_3/(FeO_T + MgO)-3*CaO-5*(K_2O/Na_2O) ternary diagram (Patiño Douce, 1999), showing source composition of monzogranitic gneisses.

Fig. 15. (A) Nb/Ta vs. Zr/Sm diagram (Foley et al., 2002), showing mostly moderate to high Nb/Ta ratios for major lithologies of Northern Hebei Province. The horizontal and vertical lines are chondritic Nb/Ta and Zr/Sm ratios of 17.6 and 25, respectively. (B) Zr/Hf vs. Lu/Hf diagram. Nearly constant and chondrite-like Zr/Hf ratios (36.3; Sun and McDonough, 1989) for most mantle-derived rocks of NHB suggest neither involvement of carbonatite metasomatism nor addition of partial melts from zircon-/detrital-rich sediments (with zircon breakdown) in the lithospheric mantle sources (Dupuy et al., 1992; Carpentier et al., 2009).

Supplementary Fig. 1. Chondrite-normalized rare earth element (REE) patterns of the dated zircon grains from amphibolite samples 13PQ07-3 (A) and 13PQ13-4 (B). Most zircon grains show parallel and magmatic zircon-like REE patterns (positive Ce and negative Eu anomalies as well as steep HREE), suggesting their crystallization from magmatic systems (Rubatto, 2002). Minor zircon grains show either higher light rare earth elements (LREEs) or lower total REE contents, possibly resulting from local element mobilization of the original magmatic zircons triggered by regional Paleoproterozoic tectonothermal events (Whitehouse and

Kamber, 2003; Wang et al., 2015b). Analyses with solid symbols are those used to calculate the crystallization ages of the magmatic precursors. The chondrite normalized values are after Sun and McDonough (1989).

Supplementary Fig. 2. Covariation diagrams of Zr versus representative (A–B) LREEs (La and Sm), (C) HFSEs (Nb), and (D-F) LILEs (Th, Ba, and Rb) for late Neoarchean basement rocks of Pingquan Complex. Generally positive correlations between Zr and La, Sm, and Nb indicate that primary igneous LREE and HFSE contents are generally preserved, whereas large scatters of Th, Ba, and Rb suggest that LILEs have been mobilized and cannot be used for petrogenetic discussions.

ACCEPTED MANUSCRIPT

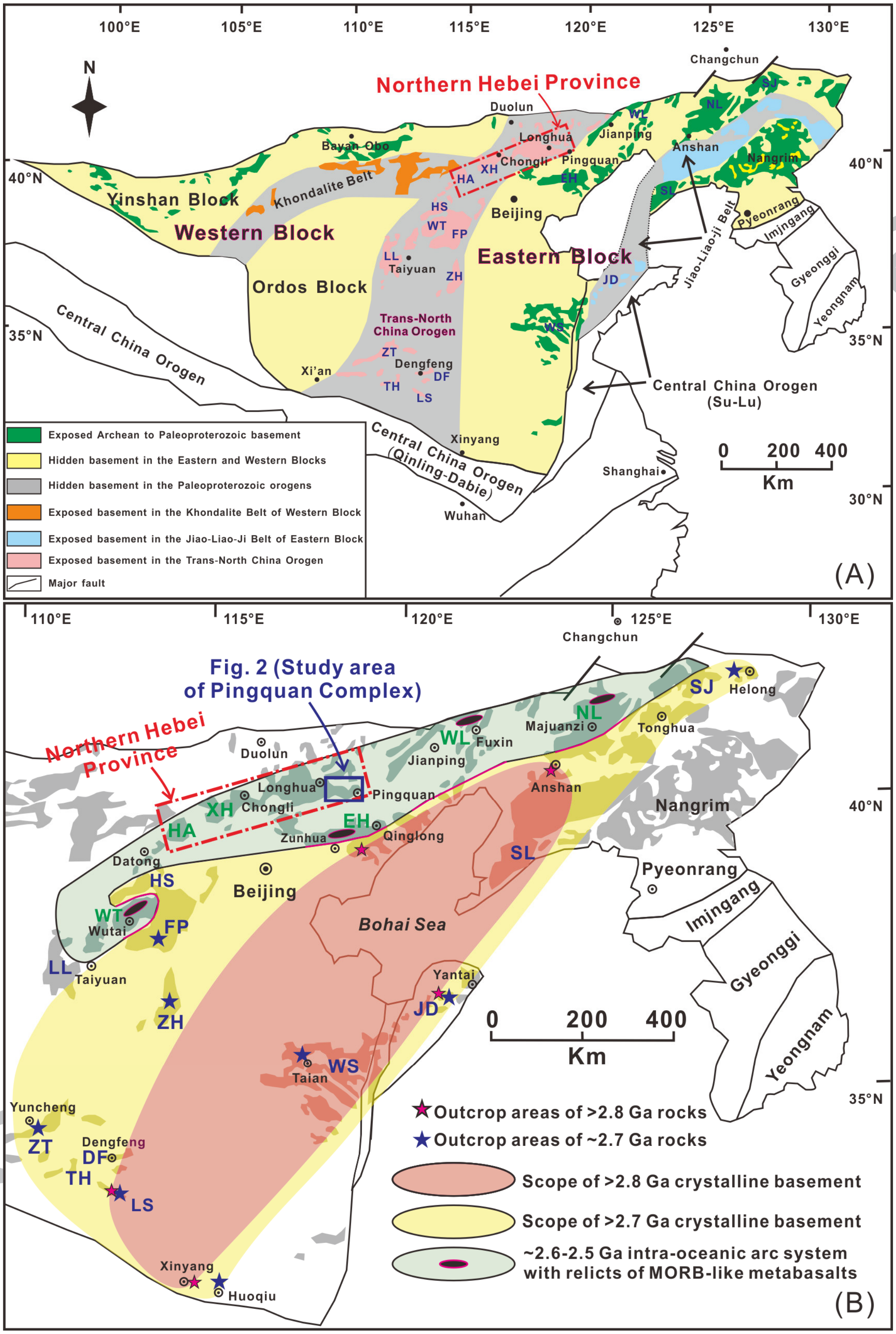

Northern Hebei Province
Yinshan Block
Western Block
Ordos Block
Khondalite Belt
Eastern Block
Trans-North China Orogen
Central China Orogen
Central China Orogen (Su-Lu)
Central China Orogen (Qinling-Dabie)
Jiao-Liao-ji Belt
Exposed Archean to Paleoproterozoic basement
Hidden basement in the Eastern and Western Blocks
Hidden basement in the Paleoproterozoic orogens
Exposed basement in the Khondalite Belt of Western Block
Exposed basement in the Jiao-Liao-Ji Belt of Eastern Block
Exposed basement in the Trans-North China Orogen
Major fault
(A)
Fig. 2 (Study area of Pingquan Complex)
Bohai Sea
Outcrop areas of >2.8 Ga rocks
Outcrop areas of ~2.7 Ga rocks
Scope of >2.8 Ga crystalline basement
Scope of >2.7 Ga crystalline basement
~2.6-2.5 Ga intra-oceanic arc system with relicts of MORB-like metabasalts
(B)

1554

1555

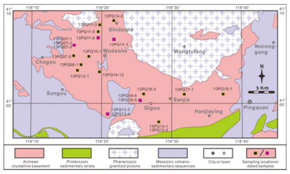
118°10′
118°20′
118°30′
118°40′
41° 10′
41° 00′
Shidaohe
Wudaohe
Wangtufang
Wolong-gang
Chagou
Sangou
Sanjia
Qigou
Hanjiaying
Pingquan
13PQ14-2
13PQ11-3
13PQ11-5
13PQ11-8
13PQ07-1
13PQ07-2
13PQ07-3
13PQ14-3
13PQ10-1
13PQ07-5
13PQ08-1
13PQ12-1
13PQ14-12
13PQ16-3
13PQ16-4
13PQ16-5
13PQ17-1
13PQ18-1
13PQ13-3
13PQ13-4
13PQ13-1
13PQ13-2
N
5 Km
Archean crystalline basement
Proterozoic sedimentary strata
Phanerozoic granitoid plutons
Mesozoic volcano-sedimentary sequences
City or town
Sampling locations/ dated samples

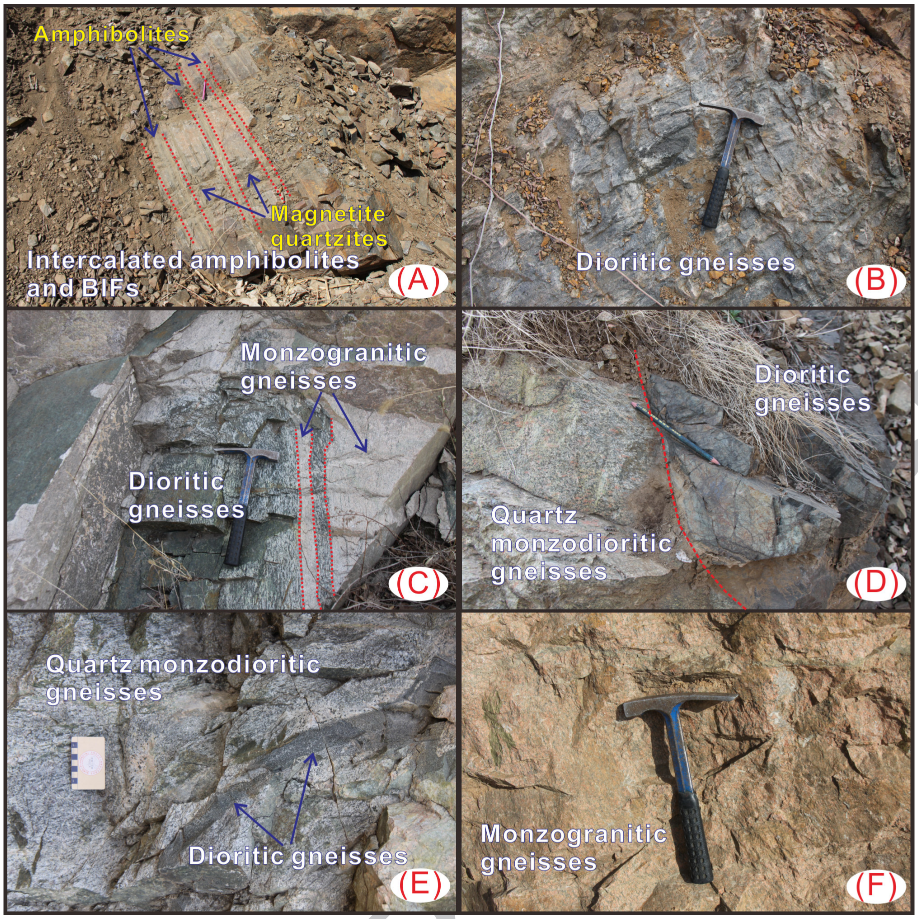
Amphibolites
Magnetite quartzites
Intercalated amphibolites and BIFs
(A)
Dioritic gneisses
(B)
Monzogranitic gneisses
Dioritic gneisses
(C)
Dioritic gneisses
Quartz monzodioritic gneisses
(D)
Quartz monzodioritic gneisses
Dioritic gneisses
(E)
Monzogranitic gneisses
(F)

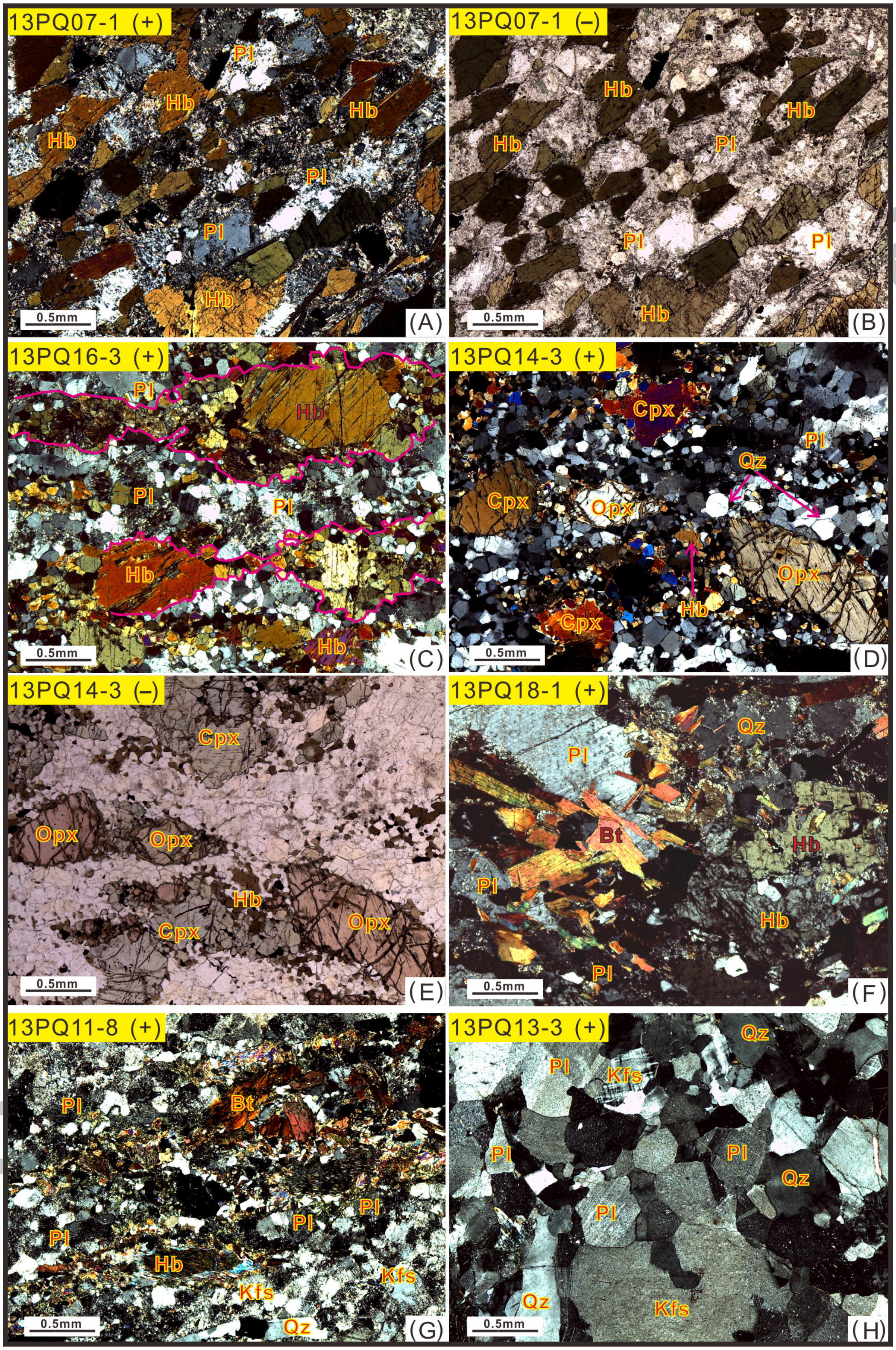

13PQ07-1 (+)
Pl
Hb
Hb
Hb
Pl
Pl
Hb
0.5mm
(A)
13PQ07-1 (–)
Hb
Hb
Hb
Pl
Pl
Pl
Hb
0.5mm
(B)
13PQ16-3 (+)
Pl
Hb
Pl
Pl
Hb
Hb
0.5mm
(C)
13PQ14-3 (+)
Cpx
Pl
Qz
Cpx
Opx
Opx
Hb
Cpx
0.5mm
(D)
13PQ14-3 (–)
Cpx
Opx
Opx
Hb
Cpx
Opx
0.5mm
(E)
13PQ18-1 (+)
Qz
Pl
Bt
Hb
Pl
Hb
Pl
0.5mm
(F)
13PQ11-8 (+)
Pl
Bt
Pl
Pl
Pl
Hb
Kfs
Kfs
Qz
0.5mm
(G)
13PQ13-3 (+)
Qz
Pl
Kfs
Pl
Pl
Qz
Pl
Qz
Kfs
0.5mm
(H)

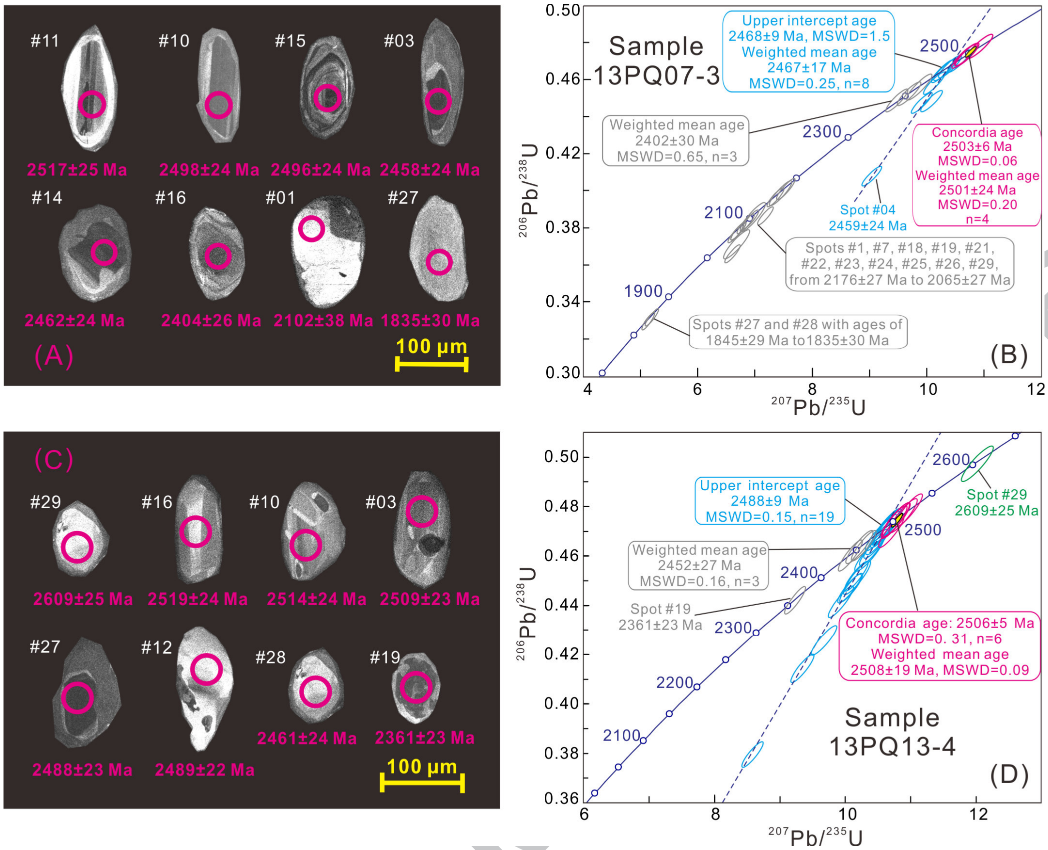

#11
#10
#15
#03
2517±25 Ma
2498±24 Ma
2496±24 Ma
2458±24 Ma
#14
#16
#01
#27
2462±24 Ma
2404±26 Ma
2102±38 Ma
1835±30 Ma
100 μm
(A)
Sample 13PQ07-3
Upper intercept age 2468±9 Ma, MSWD=1.5
Weighted mean age 2467±17 Ma MSWD=0.25, n=8
Weighted mean age 2402±30 Ma MSWD=0.65, n=3
Concordia age 2503±6 Ma MSWD=0.06
Weighted mean age 2501±24 Ma MSWD=0.20 n=4
Spot #04 2459±24 Ma
Spots #1, #7, #18, #19, #21, #22, #23, #24, #25, #26, #29, from 2176±27 Ma to 2065±27 Ma
Spots #27 and #28 with ages of 1845±29 Ma to1835±30 Ma
(B)
(C)
#29
#16
#10
#03
2609±25 Ma
2519±24 Ma
2514±24 Ma
2509±23 Ma
#27
#12
#28
#19
2461±24 Ma
2361±23 Ma
2488±23 Ma
2489±22 Ma
100 μm
Upper intercept age 2488±9 Ma MSWD=0.15, n=19
Weighted mean age 2452±27 Ma MSWD=0.16, n=3
Spot #19 2361±23 Ma
Spot #29 2609±25 Ma
Concordia age: 2506±5 Ma MSWD=0. 31, n=6
Weighted mean age 2508±19 Ma, MSWD=0.09
Sample 13PQ13-4
(D)

1562

1563

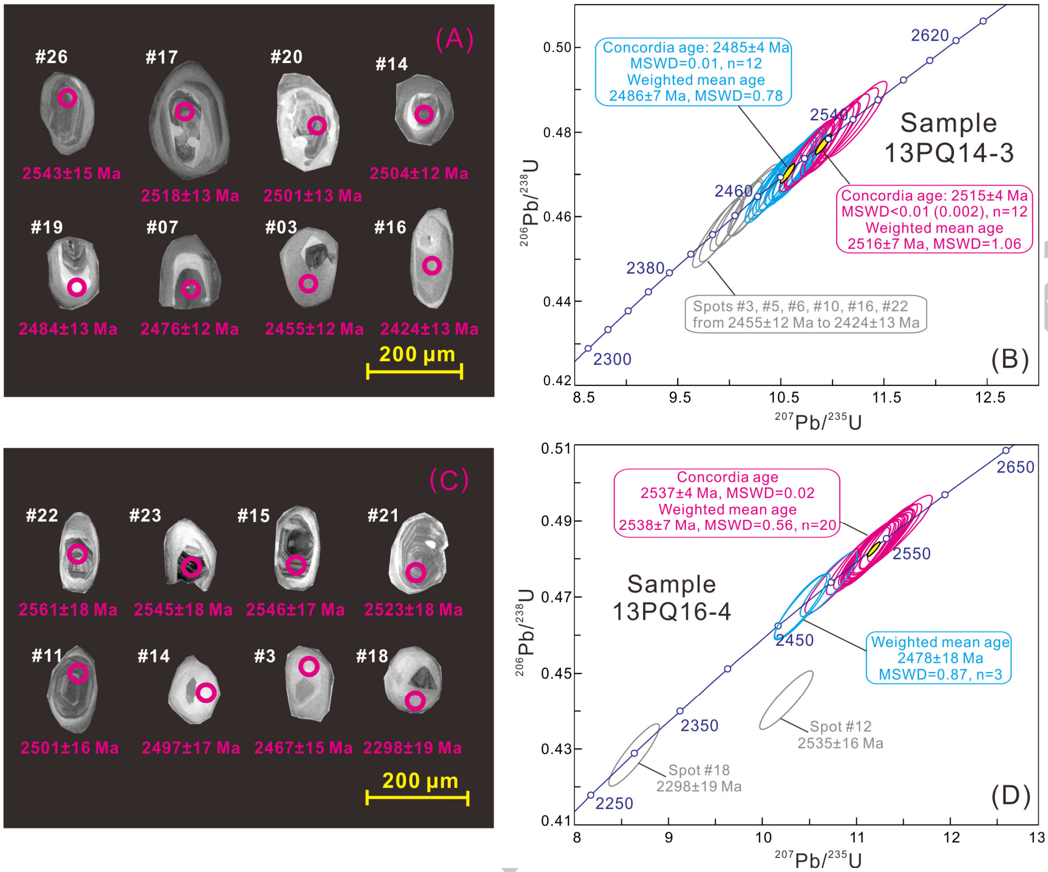
(A)
#26
#17
#20
#14
2543±15 Ma
2518±13 Ma
2501±13 Ma
2504±12 Ma
#19
#07
#03
#16
2484±13 Ma
2476±12 Ma
2455±12 Ma
2424±13 Ma
200 μm
(B)
Concordia age: 2485±4 Ma
MSWD=0.01, n=12
Weighted mean age
2486±7 Ma, MSWD=0.78
Sample
13PQ14-3
Concordia age: 2515±4 Ma
MSWD<0.01 (0.002), n=12
Weighted mean age
2516±7 Ma, MSWD=1.06
Spots #3, #5, #6, #10, #16, #22
from 2455±12 Ma to 2424±13 Ma
2620
2540
2460
2380
2300
206Pb/238U
207Pb/235U
(C)
#22
#23
#15
#21
2561±18 Ma
2545±18 Ma
2546±17 Ma
2523±18 Ma
#11
#14
#3
#18
2501±16 Ma
2497±17 Ma
2467±15 Ma
2298±19 Ma
200 μm
(D)
Concordia age
2537±4 Ma, MSWD=0.02
Weighted mean age
2538±7 Ma, MSWD=0.56, n=20
Sample
13PQ16-4
Weighted mean age
2478±18 Ma
MSWD=0.87, n=3
Spot #12
2535±16 Ma
Spot #18
2298±19 Ma
2650
2550
2450
2350
2250
206Pb/238U
207Pb/235U

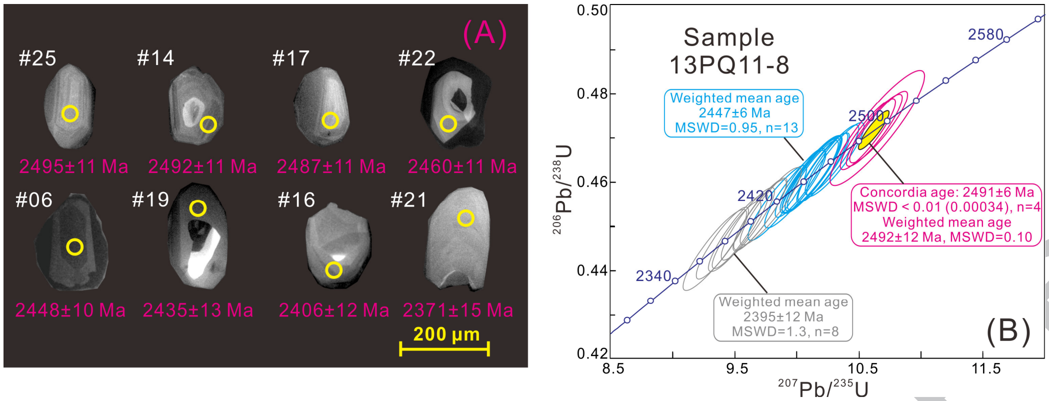
(A)
#25
#14
#17
#22
2495±11 Ma
2492±11 Ma
2487±11 Ma
2460±11 Ma
#06
#19
#16
#21
2448±10 Ma
2435±13 Ma
2406±12 Ma
2371±15 Ma
200 μm
Sample 13PQ11-8
Weighted mean age 2447±6 Ma MSWD=0.95, n=13
Concordia age: 2491±6 Ma MSWD < 0.01 (0.00034), n=4 Weighted mean age 2492±12 Ma, MSWD=0.10
Weighted mean age 2395±12 Ma MSWD=1.3, n=8
2580
2500
2420
2340
(B)
0.50
0.48
0.46
0.44
0.42
8.5
9.5
10.5
11.5
206Pb/238U
207Pb/235U

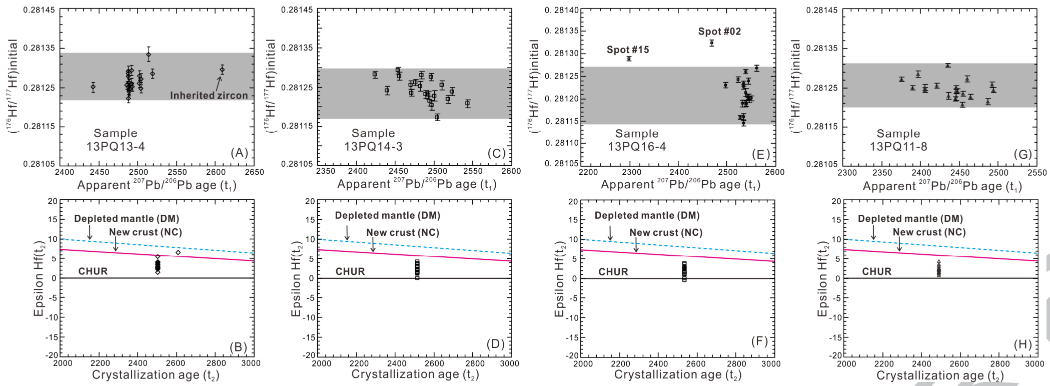
Sample
13PQ13-4
(A)
Inherited zircon
Sample
13PQ14-3
(C)
Spot #15
Spot #02
Sample
13PQ16-4
(E)
Sample
13PQ11-8
(G)
Apparent ^{207}Pb/^{206}Pb age (t$_1$)
(^{176}Hf/^{177}Hf)initial
Depleted mantle (DM)
New crust (NC)
CHUR
(B)
(D)
(F)
(H)
Epsilon Hf(t$_2$)
Crystallization age (t$_2$)

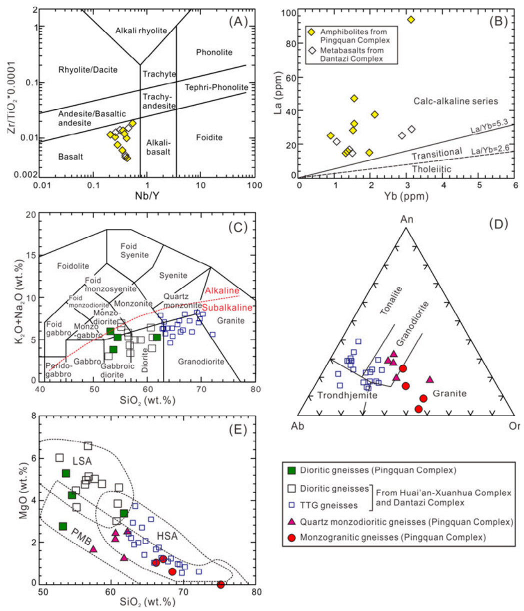
(A)
Alkali rhyolite
Rhyolite/Dacite
Trachyte
Phonolite
Tephri-Phonolite
Trachy-andesite
Andesite/Basaltic andesite
Alkali-basalt
Foidite
Basalt
Zr/TiO2*0.0001
Nb/Y
(B)
Amphibolites from Pingquan Complex
Metabasalts from Dantazi Complex
Calc-alkaline series
La/Yb=5.3
Transitional
La/Yb=2.6
Tholeiitic
La (ppm)
Yb (ppm)
(C)
Foidolite
Foid Syenite
Syenite
Foid monzosyenite
Foid monzodiorite
Monzonite
Quartz monzonite
Monzo-diorite
Alkaline
Subalkaline
Granite
Foid gabbro
Monzo gabbro
Gabbro
Gabbroic diorite
Diorite
Granodiorite
Perido-gabbro
K2O+Na2O (wt.%)
SiO2 (wt.%)
(D)
An
Tonalite
Granodiorite
Trondhjemite
Granite
Ab
Or
(E)
LSA
HSA
PMB
MgO (wt.%)
SiO2 (wt.%)
Dioritic gneisses (Pingquan Complex)
Dioritic gneisses
TTG gneisses
From Huai'an-Xuanhua Complex and Dantazi Complex
Quartz monzodioritic gneisses (Pingquan Complex)
Monzogranitic gneisses (Pingquan Complex)

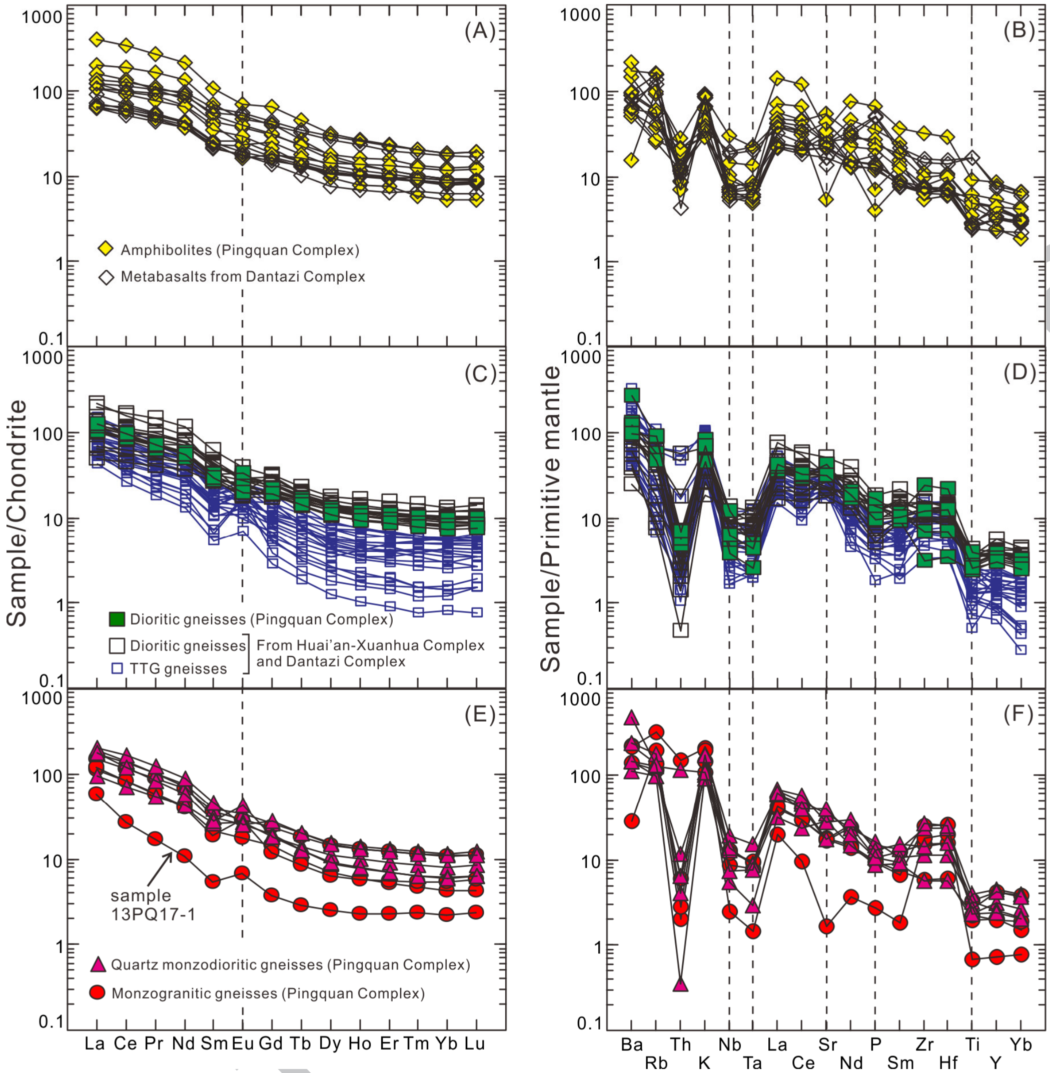

(A)
(B)
(C)
(D)
(E)
(F)
1000
100
10
1
0.1
Amphibolites (Pingquan Complex)
Metabasalts from Dantazi Complex
Sample/Chondrite
Sample/Primitive mantle
Dioritic gneisses (Pingquan Complex)
Dioritic gneisses
TTG gneisses
From Huai'an-Xuanhua Complex and Dantazi Complex
sample 13PQ17-1
Quartz monzodioritic gneisses (Pingquan Complex)
Monzogranitic gneisses (Pingquan Complex)
La Ce Pr Nd Sm Eu Gd Tb Dy Ho Er Tm Yb Lu
Ba Rb Th K Nb Ta La Ce Sr Nd P Sm Zr Hf Ti Y Yb

1572

1573

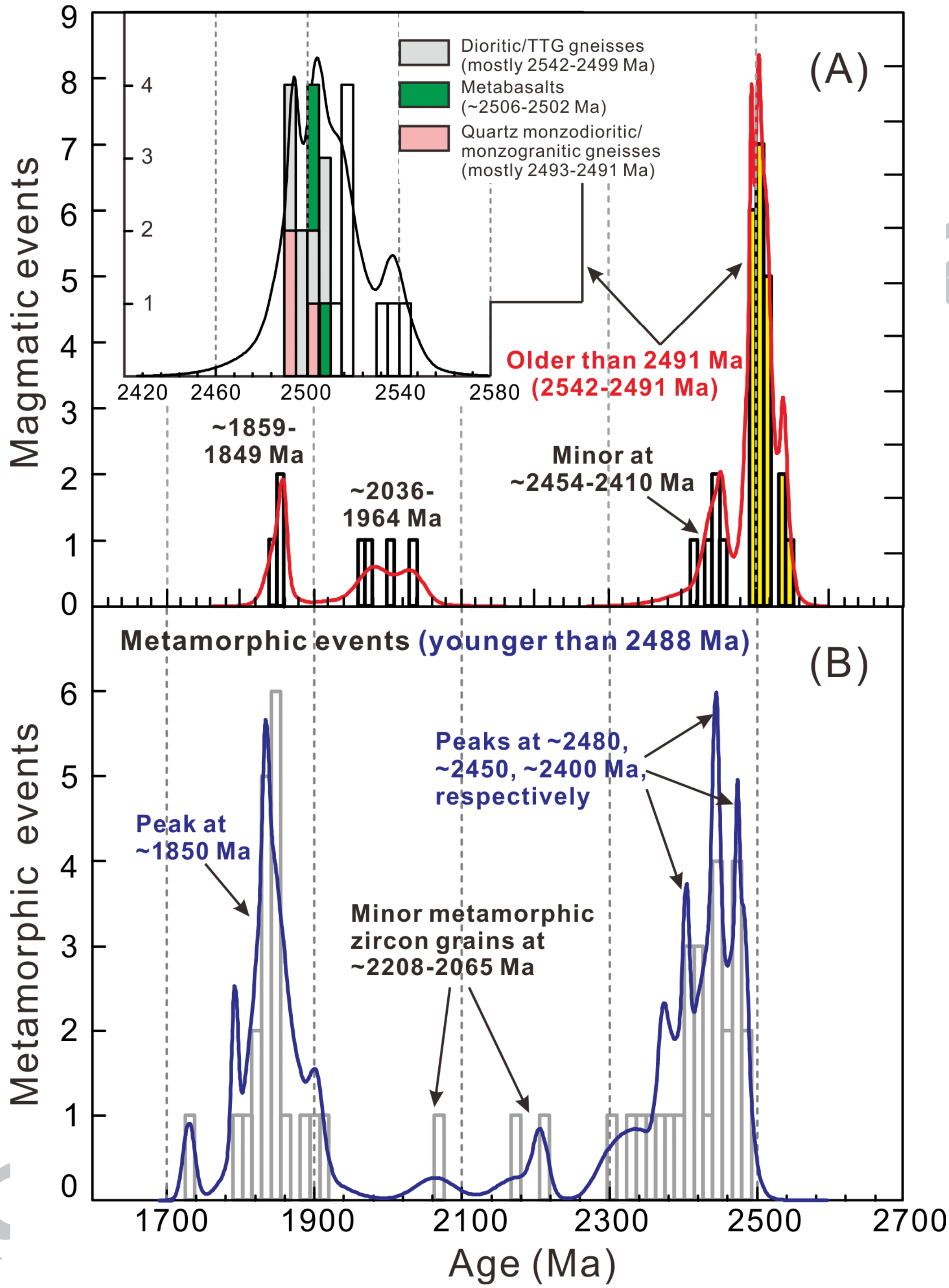

(A)
Magmatic events
Dioritic/TTG gneisses (mostly 2542-2499 Ma)
Metabasalts (~2506-2502 Ma)
Quartz monzodioritic/ monzogranitic gneisses (mostly 2493-2491 Ma)
Older than 2491 Ma (2542-2491 Ma)
~1859-1849 Ma
~2036-1964 Ma
Minor at ~2454-2410 Ma
(B)
Metamorphic events (younger than 2488 Ma)
Metamorphic events
Peak at ~1850 Ma
Peaks at ~2480, ~2450, ~2400 Ma, respectively
Minor metamorphic zircon grains at ~2208-2065 Ma
Age (Ma)

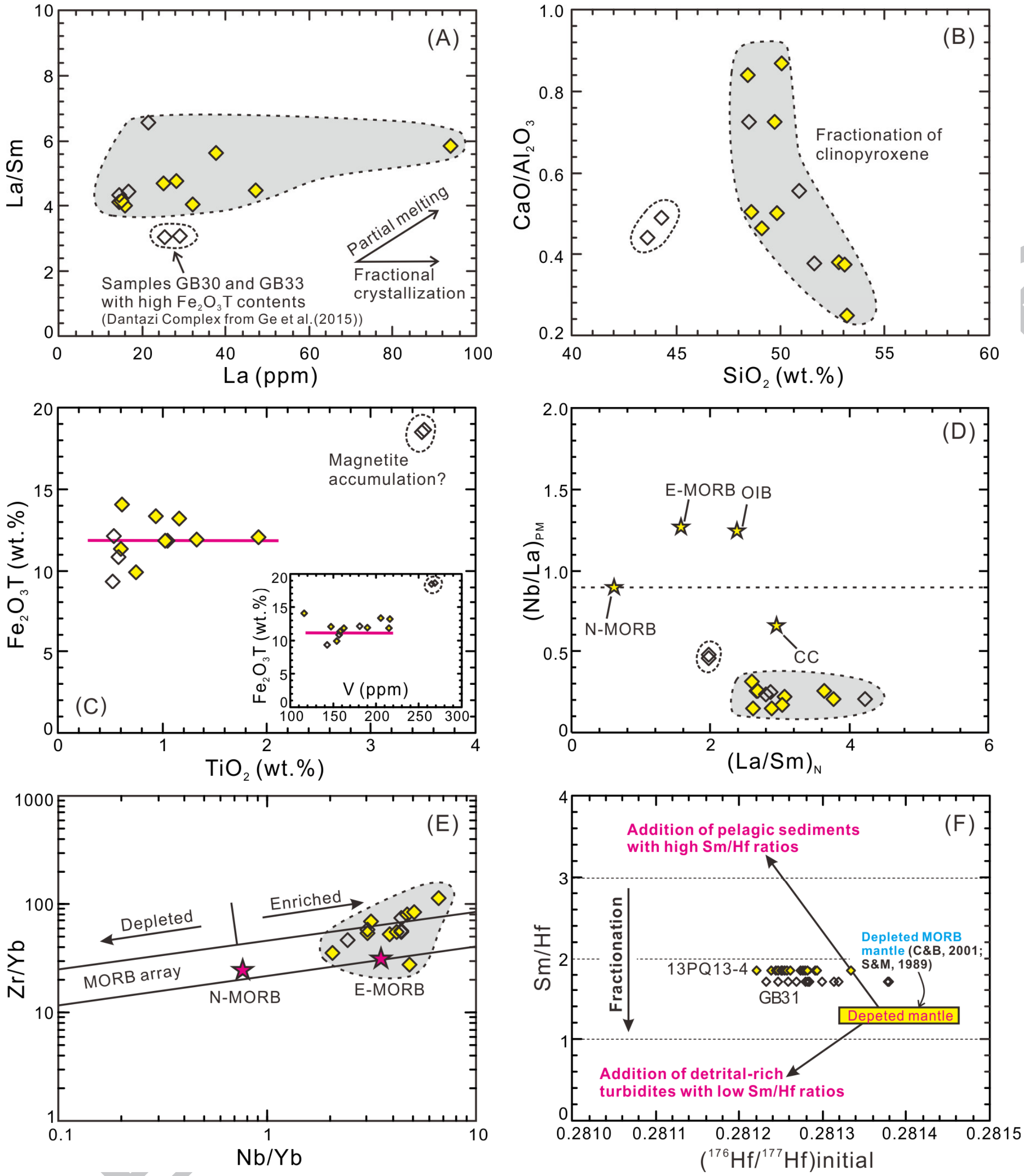

(A)
La/Sm
La (ppm)
Partial melting
Fractional crystallization
Samples GB30 and GB33 with high Fe_2O_3T contents
(Dantazi Complex from Ge et al.(2015))
(B)
CaO/Al_2O_3
SiO_2 (wt.%)
Fractionation of clinopyroxene
(C)
Fe_2O_3T (wt.%)
TiO_2 (wt.%)
Magnetite accumulation?
V (ppm)
(D)
$(Nb/La)_{PM}$
$(La/Sm)_N$
E-MORB
OIB
N-MORB
CC
(E)
Zr/Yb
Nb/Yb
Depleted
Enriched
MORB array
N-MORB
E-MORB
(F)
Sm/Hf
$(^{176}Hf/^{177}Hf)$initial
Addition of pelagic sediments with high Sm/Hf ratios
Fractionation
Depleted MORB mantle (C&B, 2001; S&M, 1989)
13PQ13-4
GB31
Depeted mantle
Addition of detrital-rich turbidites with low Sm/Hf ratios

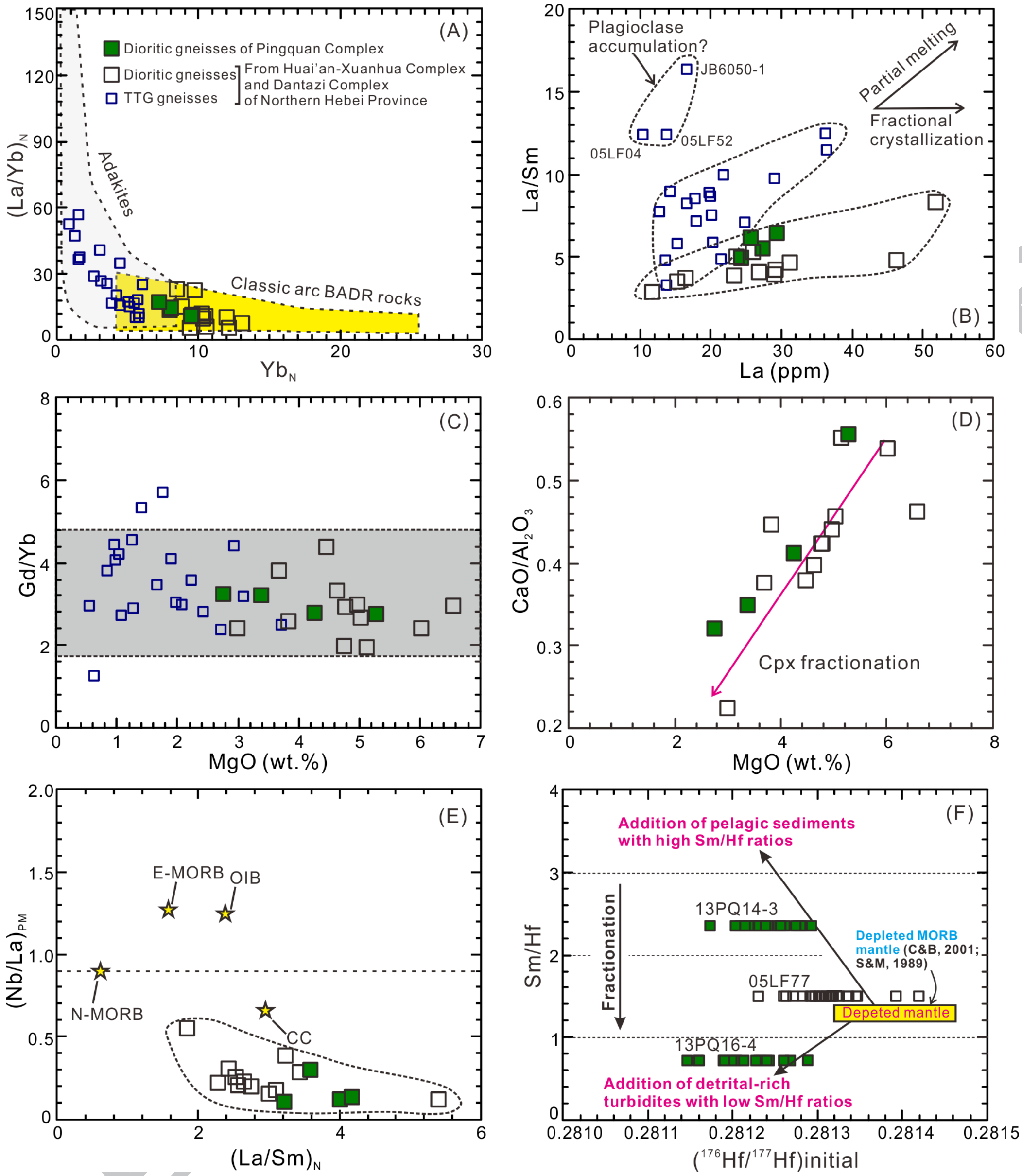
(A)
Dioritic gneisses of Pingquan Complex
Dioritic gneisses
TTG gneisses
From Huai'an-Xuanhua Complex and Dantazi Complex of Northern Hebei Province
Adakites
Classic arc BADR rocks
(La/Yb)N
YbN
(B)
Plagioclase accumulation?
JB6050-1
05LF04
05LF52
Partial melting
Fractional crystallization
La/Sm
La (ppm)
(C)
Gd/Yb
MgO (wt.%)
(D)
Cpx fractionation
CaO/Al2O3
MgO (wt.%)
(E)
E-MORB
OIB
N-MORB
CC
(Nb/La)PM
(La/Sm)N
(F)
Addition of pelagic sediments with high Sm/Hf ratios
13PQ14-3
05LF77
13PQ16-4
Fractionation
Depleted MORB mantle (C&B, 2001; S&M, 1989)
Depeted mantle
Addition of detrital-rich turbidites with low Sm/Hf ratios
Sm/Hf
(176Hf/177Hf)initial

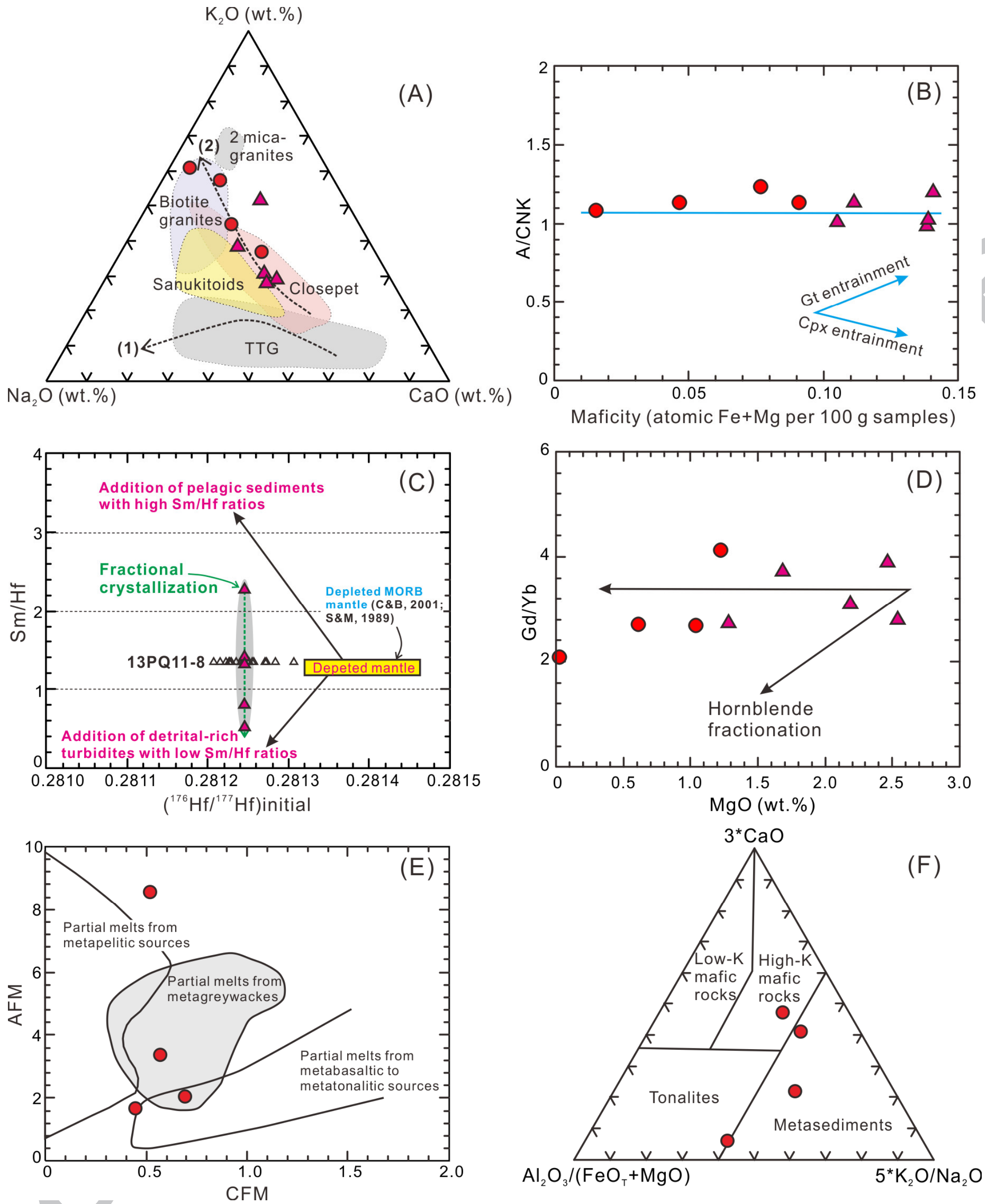
K2O (wt.%)
(A)
2 mica-
granites
(2)
Biotite
granites
Sanukitoids
Closepet
TTG
(1)
Na2O (wt.%)
CaO (wt.%)
(B)
A/CNK
Gt entrainment
Cpx entrainment
Maficity (atomic Fe+Mg per 100 g samples)
(C)
Addition of pelagic sediments
with high Sm/Hf ratios
Fractional
crystallization
Depleted MORB
mantle (C&B, 2001;
S&M, 1989)
13PQ11-8
Depeted mantle
Addition of detrital-rich
turbidites with low Sm/Hf ratios
Sm/Hf
(176Hf/177Hf)initial
(D)
Gd/Yb
Hornblende
fractionation
MgO (wt.%)
(E)
Partial melts from
metapelitic sources
Partial melts from
metagreywackes
Partial melts from
metabasaltic to
metatonalitic sources
AFM
CFM
3*CaO
(F)
Low-K
mafic
rocks
High-K
mafic
rocks
Tonalites
Metasediments
Al2O3/(FeOT+MgO)
5*K2O/Na2O

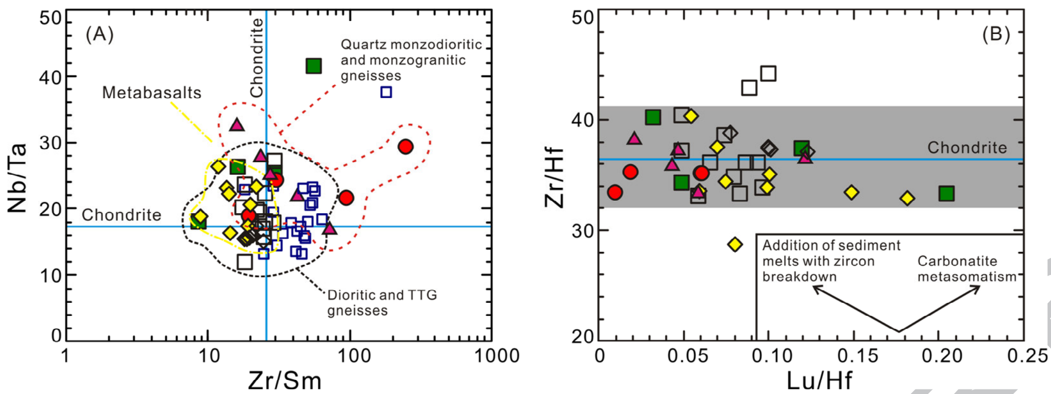
(A)
Nb/Ta
Zr/Sm
Chondrite
Chondrite
Metabasalts
Quartz monzodioritic and monzogranitic gneisses
Dioritic and TTG gneisses
(B)
Zr/Hf
Lu/Hf
Chondrite
Addition of sediment melts with zircon breakdown
Carbonatite metasomatism

Research Highlights:

- ~2537-2491 Ma Pingquan amphibolites and granitoid gneisses, Northern Hebei Province;
- Derivation from a moderately depleted mantle enriched by subducted pelagic sediments;
- Mantle heterogeneity beneath ~2.6-2.5 Ga oceanic arc along northwestern margin of EB;
- Late Neoarchean crustal growth linked to oceanic subduction and arc-continent accretion.

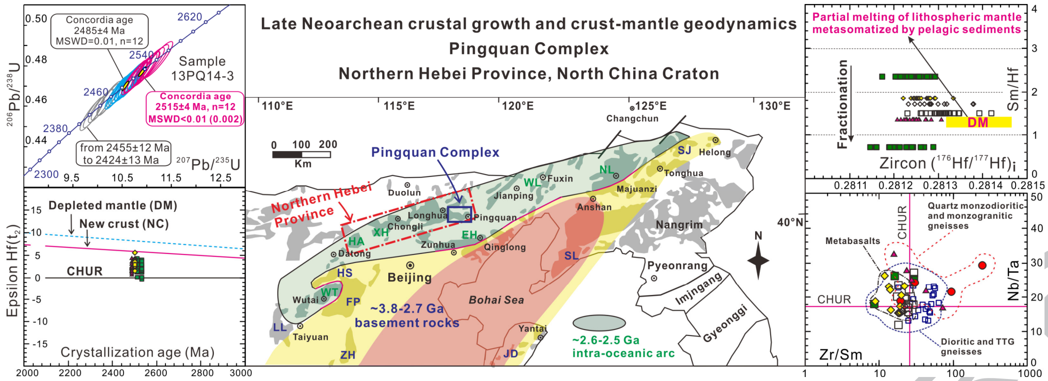

Late Neoarchean crustal growth and crust-mantle geodynamics
Pingquan Complex
Northern Hebei Province, North China Craton
Concordia age 2485±4 Ma MSWD=0.01, n=12
Sample 13PQ14-3
Concordia age 2515±4 Ma, n=12 MSWD<0.01 (0.002)
from 2455±12 Ma to 2424±13 Ma
Depleted mantle (DM)
New crust (NC)
CHUR
Epsilon Hf(t₂)
Crystallization age (Ma)
Pingquan Complex
Northern Hebei Province
Beijing
Bohai Sea
~3.8-2.7 Ga basement rocks
~2.6-2.5 Ga intra-oceanic arc
Partial melting of lithospheric mantle metasomatized by pelagic sediments
Fractionation
DM
Sm/Hf
Zircon (¹⁷⁶Hf/¹⁷⁷Hf)i
Quartz monzodioritic and monzogranitic gneisses
Metabasalts
Dioritic and TTG gneisses
Nb/Ta
Zr/Sm